

# 1 Spatially resolved single-cell multiomics map of human trophoblast 2 differentiation in early pregnancy

3  
4 Anna Arutyunyan<sup>1,2\*</sup>, Kenny Roberts<sup>1\*</sup>, Megan A Sheridan <sup>2,3\*</sup>, Ilia Kats <sup>4</sup>, Luz Garcia-  
5 Alonso <sup>1</sup>, Britta Velten <sup>1,4</sup>, Regina Hoo <sup>1</sup>, Kevin Troulé Lozano<sup>1</sup>, Louis-Francois Handfield  
6 <sup>1</sup>, Luca Marconato <sup>4,5</sup>, Elizabeth Tuck <sup>1</sup>, Lucy Gardner <sup>2,3</sup>, Cecilia Icoresi Mazzeo <sup>1</sup>, Iva  
7 Kelava <sup>1</sup>, Elena Prigmore<sup>1</sup>, Sarah A Teichmann <sup>1,5</sup> Omer Ali Bayraktar<sup>1#</sup>, Ashley Moffett  
8 <sup>2,3#</sup>, Oliver Stegle <sup>1,4,6#</sup>, Margherita Y Turco<sup># 2,3,7</sup>, Roser Vento-Tormo<sup>1, 2#</sup>

9  
10 1 Wellcome Sanger Institute, Cambridge, UK

11 2 Centre for Trophoblast Research, University of Cambridge, Cambridge, UK.

12 3 Department of Pathology, University of Cambridge, Cambridge, UK.

13 4 Division of Computational Genomics and Systems Genetics, German Cancer Research  
14 Center (DKFZ), Heidelberg, Germany

15 5 Theory of Condensed Matter, Cavendish Laboratory, Department of Physics, University of  
16 Cambridge, Cambridge, UK.

17 6 European Molecular Biology Laboratory, Genome Biology Unit, Heidelberg, Germany.

18 7 Friedrich Miescher Institute for Biomedical Research, Basel, Switzerland.

19  
20 \* co-first

21 # co-last and co-corresponding (ob5@sanger.ac.uk, am485@cam.ac.uk,  
22 oliver.stegle@embl.de, margherita.turco@fmi.ch, rv4@sanger.ac.uk)

## 25 **Abstract**

26  
27 The relationship between the human placenta, the extraembryonic organ built by the fetus,  
28 and the decidua, the mucosal layer of the uterus, is essential to nurture and protect the fetus  
29 during pregnancy. Extravillous trophoblast cells (EVTs) anchor the placenta and infiltrate the  
30 decidua, transforming the maternal arteries into high conductance vessels. Defects in  
31 trophoblast invasion and arterial transformation established during early pregnancy underlie  
32 common pregnancy disorders such as pre-eclampsia. Despite its importance, how EVT  
33 invasion is regulated in humans is still unclear due the inaccessibility of the entire pregnant  
34 uterus and, until recently, a lack of reliable *in vitro* models. Here, we have generated a  
35 spatially-resolved multiomics single-cell atlas of the entire maternal-fetal interface including  
36 the myometrium, allowing us to resolve the full trajectory of trophoblast differentiation. We  
37 have used this cellular map to elucidate the main regulatory programmes mediating EVT  
38 invasion and show that they are preserved in trophoblast organoids. We define the  
39 transcriptomes of the final cell states of trophoblast invasion: placental bed giant cells (fused  
40 multinucleated EVTs) and endovascular EVTs (which form plugs inside the maternal arteries).  
41 We reconstruct the cell-cell communication events contributing to trophoblast invasion and  
42 GC formation, and define the dual role of interstitial EVTs and endovascular EVTs in mediating  
43 arterial transformation during early pregnancy. Together, our data provides a comprehensive  
44 analysis of postimplantation trophoblast differentiation in humans that can be used as a  
45 blueprint to design accurate multilineage placental *in vitro* models.

46

47 During the nine months of human pregnancy the fetus is entirely dependent on its placenta.  
48 This transient extra-embryonic organ is located at the interface between the mother and her  
49 fetus. Trophoblast is the main cell type of the placenta, and arises from the trophectoderm  
50 surrounding the preimplantation embryo<sup>1</sup>. After implantation, extravillous trophoblast cells  
51 (EVTs) emerge from the cytotrophoblast shell, infiltrate the decidua, the mucosal layer of the  
52 pregnant uterus, and migrate towards the spiral arteries where they destroy the smooth  
53 muscle media. Subsequently, endovascular trophoblast cells (eEVTs) form a plug close to the  
54 cytotrophoblast shell where the arteries terminate and replace the endothelium<sup>2</sup>. In this way  
55 EVT<sup>s</sup> transform maternal arteries in the decidua basalis into high conductance vessels<sup>3-6</sup>.  
56 EVT<sup>s</sup> begin to fuse into placental bed giant cells (GCs) deeper in the decidua and eventually  
57 migrate as far as the inner third of the myometrium<sup>7</sup>.

58  
59 Defects in decidualisation are associated with pre-eclampsia<sup>8</sup>, a syndrome characterised by  
60 defective arterial transformation by EVT<sup>s</sup>. In contrast, excessive invasion of EVT<sup>s</sup> into the  
61 uterus occurs when the decidua is missing (for instance at a scar from a previous caesarean  
62 section) and can even cause uterine rupture<sup>9</sup>. Thus, placentation and successful pregnancy  
63 depends on the correct degree of trophoblast invasion, and the decidua plays an important  
64 role. Both trophoblast cell-intrinsic mechanisms (i.e. precisely coordinated gene expression  
65 as EVT<sup>s</sup> invade) and signals provided by the surrounding maternal decidual cells contribute  
66 to this crucial process.

67  
68 Investigating the human maternal-fetal interface early in pregnancy is hampered by ethical  
69 and logistical limitations because samples can only be obtained from voluntary terminations  
70 of pregnancy. Moreover, animal models are of limited use in modelling the particularly invasive  
71 haemochorial type of placentation characteristic of humans, which is distinct even from other  
72 primates apart from great apes<sup>10</sup>. Primary trophoblast organoids are able to recapitulate some  
73 aspects of placental development and invasion<sup>11-13</sup> but their accuracy at the single-cell level  
74 remains to be determined. Our previous single-cell transcriptomics analysis of the first  
75 trimester maternal-fetal interface has provided an unprecedented view of the cell states  
76 comprising this environment<sup>14</sup>. However, the full spectrum of trophoblast states is not likely to  
77 be captured in existing single-cell transcriptomics atlases<sup>14,15</sup> due to the absence of certain  
78 trophoblast subsets from decidual and placental tissue cell isolates. In particular, trophoblast  
79 cells present in the deeper layers of the decidua and myometrium are absent from standard  
80 surgical samples, and the villous syncytiotrophoblast (SCT), a multinucleated layer, is lost in  
81 classical single-cell RNA sequencing (scRNA-seq). A further difficulty is the loss of spatial  
82 context in these samples, which is essential to systematically resolve the interactions between  
83 trophoblast and decidual cells in early pregnancy.

84  
85 Single-cell and spatial transcriptomic atlases of tissues have been transformative in  
86 understanding human development<sup>16-19</sup>, mapping disease<sup>20,21</sup> and engineering organoids<sup>22,23</sup>.  
87 Here, we present a spatially-resolved single-cell multiomics characterization of the maternal-  
88 fetal interface. We examine the site of placentation from historical samples of first trimester  
89 hysterectomies, which include the entire uterus containing the placenta, decidua and  
90 myometrium. To faithfully recapitulate the dynamics of trophoblast invasion, we developed  
91 StOrder, a computational and statistical framework that reconstructs the smooth transition of  
92 cell states in space. Spatiotemporal ordering of trophoblast invasion allows us to characterise  
93 the molecular processes underpinning trophoblast invasion. We use this comprehensive  
94 detailed account of trophoblast differentiation to benchmark our trophoblast organoid model<sup>11</sup>.

95 Using our tool CellPhoneDB v4<sup>18</sup>, we describe interactions between trophoblast subsets and  
96 decidual cells that are likely to affect how trophoblast transformation of arteries occurs in early  
97 pregnancy. Thus, we provide a description of the whole trajectory of human trophoblast cell  
98 states and their spatial niches.

99

100 **Spatiotemporal map of the placental-decidual interface defines four villous**  
101 **cytotrophoblast subsets**

102

103 We profiled three human implantation sites (between 6 and 9 post-conceptional weeks, PCW)  
104 using a multimodal approach (**Fig. 1a-c, Supplementary Tables 1-3**). Consecutive sections  
105 from frozen tissue blocks of the implantation site were used for: (i) single-nuclei RNA  
106 sequencing (snRNA-seq); (ii) combined single nuclei RNA and ATAC sequencing (snRNA-  
107 seq/snATAC-seq, further referred to as multiome); and (iii) spatial transcriptomics using  
108 Visium. To account for the large tissue area of one donor (P13), we targeted four consecutive  
109 sections with four spatial transcriptomics capture areas (**Supplementary Fig. 1a**). We also  
110 profiled five decidual and three placental samples from 8-13 PCW by scRNA-seq/snRNA-seq  
111 and integrated all the data with our previous scRNA-seq dataset of the maternal-fetal  
112 interface<sup>14</sup> (**Fig. 1d, Supplementary Fig. 2a-e**). Our single-cell and spatial transcriptomics  
113 map is available at [reproductivecellatlas.org](http://reproductivecellatlas.org).

114

115 We examined trophoblast heterogeneity in two steps. Firstly, we analysed the full-thickness  
116 implantation site from P13 (~9 PCW), as it contains both fetal (placenta) and maternal (decidua  
117 and myometrium) tissues on the same slide, and the tissue block is perfectly preserved and  
118 oriented (**Fig. 1e, Supplementary Fig. 3a**). Secondly, we validated the trophoblast  
119 populations and their markers in the integrated dataset (~8-13 PCW) (**Supplementary Fig.**  
120 **3b-c**). Trophoblast subsets were annotated by considering canonical markers and their spatial  
121 location (**Fig. 1f-g, Supplementary Fig. 1a-b, 3c**). To assign spatial coordinates we used  
122 cell2location<sup>24</sup>, our probabilistic method to deconvolve the spatial voxels using our pre-defined  
123 snRNA-seq data (**Fig. 1f, Supplementary Fig. 1a-b**). We then placed the trophoblasts into  
124 five pre-defined microenvironments (ME) in the tissue based on manual histological  
125 annotation.

126

127 In the placental villi (ME1), villous cytotrophoblasts (VCTs) fuse to form the overlying SCT  
128 layer that is in contact with maternal blood in the intervillous space. VCT subsets express high  
129 levels of the TFs *TP63* and *CDH1* in P13 donor (**Fig. 1g**) and the rest of the donors  
130 (**Supplementary Fig. 3d**). VCT and VCT proliferative (VCT-p) upregulate known stem  
131 cell/progenitor markers (*LGR5*, *L1TD1*, *TP63*), WNT-signalling molecules (*WLS*, *TNIK*, *LRP2*),  
132 the *SEMA3F-NRP2* signalling complex, and the VCT marker *BCAM*<sup>25</sup> (**Fig. 1h**,  
133 **Supplementary Fig. 3e**). We define an additional population of VCTs in the placental villi that  
134 we name VCT-fusing which the connectivity network PAGA<sup>26</sup> indicates is an intermediate cell  
135 state between VCT and SCT (**Supplementary Fig. 3f**). As VCT commit into VCT-fusing, they  
136 downregulate WNT (*WLS*, *TNIK*, *LRP2*) and BMP signals (*BMP7*, and upregulation of BMP  
137 antagonist *GREM2*), and upregulate the endogenous retroviral genes (*ERVW-1*, *ERVFRD-1*,  
138 *ERVV-1*) known to mediate trophoblast fusion (**Fig. 1h, Supplementary Fig. 3e**)<sup>27</sup>. Our nuclei  
139 isolation strategy allows capture of mature multinucleated SCT (*CYP19A1*, *MFSD2A*) not  
140 found in previous scRNA-seq studies<sup>14,15</sup> (**Fig. 1g, Supplementary Fig. 3d**).

141

142 Foci of cytotrophoblast cell columns arise from the VCTs that break through the SCT. These  
143 expand and form a shell around the conceptus which becomes discontinuous in the following  
144 weeks. EVTs begin to differentiate in cell columns but invasive EVTs only emerge when the  
145 villi attach to the maternal decidua as anchoring villi. In the trophoblast shell (ME2), we define  
146 an additional population of cytotrophoblast cell column VCT (VCT-CCC) (**Fig. 1f, Supplementary Fig. 1b**). VCT-CCC are proliferative and PAGA analysis shows they are likely  
147 to emerge from VCT/VCTp and give rise to EVT (**Supplementary Fig. 3f**). This analysis  
148 suggests VCT is a common progenitor for both VCT-fusing, giving rise to SCT in the placenta,  
149 and VCT-CCC where EVTs emerge. As they commit into VCT-CCC, they downregulate WNT  
150 (*WLS*, *TNIK*, *LRP2*), upregulate *NOTCH1*<sup>28,29</sup>, perform an integrin shift (upregulating *ITGB6*  
151 and *ITGA2*), and upregulate markers characteristic of the epithelial-mesenchymal transition  
152 (EMT) programme (*LPCAT1*<sup>30</sup>) (**Fig. 1h, Supplementary Fig. 3e**). Expression of *NOTCH1*  
153 and *ITGA2* is characteristic of trophoblast progenitor cells located in the column niche<sup>28,29</sup>. In  
154 agreement with this finding, in ME2, VCT-CCC co-localise with EVT (**Fig. 1f, Supplementary**  
155 **1b**). Altogether, our single-cell transcriptomics atlas defines the markers of a VCT population  
156 that can differentiate into VCT-fusing (progenitors of SCT) and is also likely to give rise to  
157 VCT-CCC (progenitors of EVTs).  
158

159

## 160 **StOrder defines the invasion trajectory of EVTs into the decidua**

161

162 To further investigate the EVT differentiation pathway as it arises from the cytotrophoblast cell  
163 columns of the anchoring villi to infiltrate maternal tissue, we leveraged both single-cell and  
164 spatial transcriptomics data using a three-step statistical framework, which we named StOrder  
165 (**see Methods**). Firstly, StOrder builds a gene expression-based connectivity matrix  
166 (generated in our case by PAGA<sup>26</sup>) to establish putative connections between clusters. The  
167 values in this matrix are interpreted as pairwise similarity scores for cell states in the gene  
168 expression space (**Fig. 2a, Supplementary Fig. 4a**). Secondly, StOrder generates a spatial  
169 covariance matrix that reflects pairwise proximity of trophoblast states that co-exist in space.  
170 To do so, StOrder takes as an input the estimated cell densities per spot (derived in our case  
171 with cell2location<sup>24</sup>) in Visium spatial transcriptomics data, and fits a Gaussian Process model  
172 that derives pairwise spatial covariance scores for all the cell state pairs (**Fig. 2a**). This allows  
173 inference of which cell states are proximal in physical space and are likely gradually  
174 differentiating as they migrate. Third, StOrder reconstructs connections between cell states by  
175 summing the connectivity matrix (step 1) from single-cell transcriptomics data and the spatial  
176 covariance matrix (step 2) from the spatial data in a weighted manner (**Fig. 2a, Supplementary Fig. 4b-d**). In sum, StOrder reconstructs the likely cell transitions in space by  
177 taking into account both the single-cell transcriptomics and the mini-bulk spatial  
178 transcriptomics data.  
179

180

181 StOrder allowed us to resolve the most likely trajectory for the emergence and differentiation  
182 of invasive EVTs (**Fig. 2a**). VCT-CCC are the precursors of EVTs-1 and EVTs-2, which co-  
183 localise with VCT-CCC in ME2 (**Fig. 1f, Supplementary 1b**). EVT-1 are proliferative and  
184 closely related to VCT-CCC, while EVT-2 do not proliferate and have an early invasive  
185 phenotype, upregulating the metalloprotease *ADAMTS20* and the fibronectin-binding integrin  
186 *ITGA1* (**Fig. 1g, Supplementary Fig. 3d**). EVT-2, located at the distal end of the columns of  
187 the anchoring villi, is identified as the bifurcation point (**Fig. 2a**). EVT-2 can either transition  
188 into iEVTs, located in the invasion front of the decidua, or eEVTs, located inside the arteries.  
189 In agreement with eEVTs emerging from the tips of the columns, we detect spontaneous

190 appearance of *NCAM1*+ cells on a small number of EVTs in the cell columns (**Supplementary**  
191 **Fig. 5**).

192  
193 Highly invasive interstitial EVTs (iEVts) are found in ME3, between decidual stromal and  
194 immune cells (**Fig. 1f**). iEVts upregulate *PLAC8*<sup>31</sup> and plasminogen activator inhibitors,  
195 *SERPINE1* and *SERPINE2*, with concomitant downregulation of plasminogen activator  
196 (*PLAU*) (**Fig. 1g, Supplementary Fig. 3d**). iEVts eventually fuse to form placental bed GCs  
197 deeper in the decidua and myometrium (ME4). GCs upregulate *RAC1* and *CD81*, both  
198 involved in myoblast fusion<sup>32,33</sup>, and the *PRG2-PAPPA* complex<sup>34</sup> (**Fig. 1f-g, Supplementary**  
199 **Fig. 3c, Supplementary Fig. 1b**). eEVts, likely emerging from EVT-2, are present inside  
200 spiral arteries (ME5) (**Supplementary Fig. 3a**). eEVts express *CD56* (*NCAM1*)<sup>35,36</sup> and also  
201 upregulate the antioxidant enzyme *GGT1*, the liprin-associated member *PPFIA4*, and the  
202 metalloproteinase *MMP12* (**Fig. 1g, Supplementary Fig. 3d**).

203  
204 We next explored the regulatory programmes mediating EVT invasion by analysing the  
205 multimodal RNA-ATAC data (**Supplementary Fig. 4e-g**). We applied our multifactorial  
206 method MEFISTO<sup>37</sup> to donor P13 multimodal data, which contained the full spectra of VCT  
207 and EVT subsets (**Fig. 2b-c, Supplementary Fig. 4h-i**). MEFISTO identified 10 latent factors  
208 that jointly explain 12.5% and 3% of the variance in the RNA expression data and the  
209 chromatin accessibility respectively (**Fig. 2c, Supplementary Fig. 4j, see Methods**). Using a  
210 logistic regression approach, we define factors 2, 4, 6 and 10 as the main driving factors of  
211 the trophoblast trajectory (**Fig. 2d, Supplementary Fig. 4k-l**). Factors 2, 4 and 6 explain  
212 changes along the main trophoblast invasion streak (VCTs-CCC through to GCs)  
213 (**Supplementary table 4**). Genes contributing strongly to these factors are *MKI67*, *CENPK*  
214 (cell cycle, factor 2); *CSF1R*<sup>38</sup>, *ADAM8*, *LAIR2*<sup>39</sup> (early trophoblast invasion, factor 4); *CALD1*,  
215 *COL21A1* (late trophoblast invasion, factor 6). Factor 10 captured eEVts; the main genes  
216 contributing to this factor include *NCAM1*, *JAG1*, *ADORA1*, *EPHA1* and *HES4*.

217  
218 **Transcription factor changes driving trophoblast fate during invasion**

219  
220 To identify the major regulatory programmes driving EVT differentiation, we extracted the  
221 transcription factors (TFs) that are differentially expressed and active along the EVT  
222 differentiation trajectory (**Supplementary Table 5**). In addition, we included TFs whose  
223 binding motifs were enriched in top ATAC features of factors 2, 4, 6 and 10 in our multimodal  
224 analysis using MEFISTO (**Supplementary Table 5**). As expected, activation of NOTCH  
225 (*HEY1*, *FOXM1*, *NOTCH1*) triggers differentiation of VCTs into VCT-CCC<sup>28</sup> (**Fig. 2e**). As  
226 previously shown, upregulation of *NOTCH1* may lead to the reduction of *IRF6* and *TP63*  
227 expression characteristic of VCT-CCC<sup>28,40</sup>. VCT-CCC upregulate the non-canonical NF-*κB*  
228 pathway (*NFKB2*, *BACH2*) and AP-1 factors (*FOSL1*, *JUN*, *JDP2*, *ATF3*), that may trigger the  
229 EMT program (e.g. upregulation *SNAI1*) (**Fig. 2e**). Activation of the non-canonical NF-*κB*  
230 pathway is maintained throughout EVT differentiation, but there is upregulation of the NF-*κB*  
231 inhibitor (*NFkBIZ*) at the iEVT stage (**Fig. 2e**). This could be a mechanism to avoid  
232 inflammation as EVTs invade<sup>14</sup>.

233  
234 Decidual stromal cells secrete the WNT inhibitor *DKK1*<sup>23</sup> and EVT invasion is marked by strong  
235 inhibition of WNT, with downregulation of the WNT target *AXIN2* and upregulation of the WNT  
236 repressor *CSRN1P1* in iEVts (**Fig. 2e-f**). In addition, iEVts upregulate TFs involved in cancer  
237 invasion (*ELK3-GATA3* complex<sup>41</sup>) and tumour suppressor genes (*ELF4*, *GRHL1*), in keeping

238 with iEVTs being non-proliferative (**Fig. 2e**). As iEVTs transition into GCs, they upregulate the  
239 type I IFN pathway, including TFs (*IRF7*, *STAT1*, *STAT2*), downstream transducers (*JAK1*),  
240 and targets (*IFI27*) (**Fig. 2e-f**). These results suggest that type I IFN might play a role in GC  
241 fusion.

242  
243 Following implantation and the formation of eEVT plugs in the spiral arteries, before 10 PCW  
244 the placenta is in a physiologically low-oxygen environment<sup>42</sup>. The hypoxia-inducible HIF1a  
245 pathway (*HIF1A*, *ARNT*, *STAT3*) is upregulated in both iEVTs and eEVTs but the HIF1A target  
246 *EIF4E1B*<sup>43</sup> is upregulated only in eEVTs, pointing to a role for this pathway in eEVT fate (**Fig.**  
247 **2e-f**). eEVTs also upregulate the NOTCH pathway (*HES4*, *JAG1*) and *GATA6*, both of them  
248 lowly expressed in iEVT. *GATA6* is known to affect vessels by suppressing autocrine TGF $\beta$   
249 signalling<sup>44</sup> and may have a similar role in this context, with both *TGFB1* and its receptor  
250 *TGFBR1* downregulated in eEVTs. This is different from iEVT, where both *TGFB1* and  
251 *TGFBR1* are upregulated. Additional TFs involved in the hypoxic environment in tumours and  
252 vessel transformation are upregulated in eEVTs, including *HMGA2*<sup>45</sup>, *PAX8*<sup>46</sup>, *PBX3*<sup>47</sup>,  
253 *PLAGL1*<sup>48</sup> and *MYCN*.

254  
255 To summarise, our results point towards a key role for WNT inhibition, TGF $\beta$  and HIF1A  
256 activation in iEVT cell fate, while eEVT identity is marked by strong upregulation of NOTCH  
257 and HIF1A and strong downregulation of TGF $\beta$  signalling (**Fig. 2g**).  
258

## 259 **Invasive trophoblast subsets are recapitulated in tissue-derived placental organoids**

260

261 We next explored if the cell-intrinsic regulatory programme that is triggered upon VCT-to-EVT  
262 differentiation is also present in our trophoblast organoids<sup>11</sup>. Our organoids are derived from  
263 primary placental cells and recapitulate the spontaneous fusion of VCT into SCT *in vitro*.  
264 Changing from trophoblast organoid medium (TOM) to EVT medium (EVTM) induces an  
265 invasive phenotype<sup>11,49</sup>. We differentiated organoids from six donors into EVTs and collected  
266 samples at 3h, 24h, 48h and 96h from the start of differentiation (**Fig. 3a-b**). Organoids from  
267 both experiments were integrated into the same manifold and analysed in concert (**Fig. 3c**,  
268 **Supplementary Fig. 6a**). To define the identity of trophoblast states within the organoids, we  
269 first plotted the unique trophoblast markers identified in our *in vivo* atlas (**Supplementary Fig.**  
270 **6b-c**). Additionally, we projected the trophoblast *in vivo* reference data onto the *in vitro*  
271 trophoblast subsets by building a logistic regression classifier that we trained on the donor  
272 P13 trophoblast dataset<sup>23</sup> (**Fig. 3d**, **Supplementary Fig. 6d**).  
273

274 We resolved the four VCT subsets identified *in vivo* in our trophoblast organoids. In the  
275 presence of TOM, the organoids were enriched in VCT (*LGR5*, *L1TD1*, *TP63*, *WLS*, *TNIK*,  
276 *LRP2*, *SEMA3F*, *NRP2*, *BCAM*) and VCT-fusing (*ERVW-1*, *ERVFRD-1*, *ERVV-1*, *GREM2*)  
277 (**Fig. 3c-f**, **Supplementary Fig. 6e**). In our organoid dataset, SCT are *CYP19A1*-low and  
278 *MEFSD2A*-low, in agreement with the failure to capture fully differentiated multinucleated SCT  
279 by scRNA-seq (**Fig. 3g**). A population of VCT-CCC (*ITGB6*, *LPCAT1*, *NOTCH1*, *ITGA2*)  
280 appeared only in the presence of EVTM (**Fig. 3f**). EVTs emerge from VCT-CCC, suggesting  
281 that both *in vivo* and *in vitro*, VCTs have the potential to differentiate into either SCT or EVT  
282 lineages. These results suggest that cell fate shifts of VCT subsets are modulated by the  
283 culture conditions in *in vitro* trophoblast.

284

285 EVT populations arising in the presence of EVTM media were assigned as EVT. Despite some  
286 differences between the EVT subsets *in vivo* and *in vitro* (probability < 0.6), we find a small  
287 population in the organoids that corresponds to *in vivo*-iEVTS with a high probability score  
288 (probability > 0.8) (**Fig. 3d-e, Supplementary Fig. 6d**). *In vitro*-iEVTS are enriched in later  
289 stages (48h and 96h), as expected, and are only present in two of the donors (**Supplementary**  
290 **Fig. 6e**). Like their *in vivo* counterparts, iEVTS upregulate the plasminogen activator inhibitors  
291 *SERPINE1* and *SERPINE2* and downregulate *PLAU*. No expression of *NCAM1* is seen in  
292 differentiated organoid cultures, indicating the absence of eEVTS (**Fig. 3g**). To further  
293 demonstrate the similarities between iEVTS *in vivo* and *in vitro*, we mapped *in vitro*-iEVTS onto  
294 the *in vivo* spatial transcriptomics data using cell2location<sup>24</sup>. *In vitro*-iEVTS exhibit a strong  
295 degree of localization to ME3 *in vivo* (Spearman rank-order correlation coefficient 0.91, p-  
296 value < 10e-308, two-sided test) (**Fig. 3h, Supplementary Fig. 6f-g, Supplementary Table**  
297 **6**). This demonstrates the presence of invading iEVTS in our trophoblast organoid model and  
298 their suitability to study mechanisms modulating trophoblast invasion.  
299

300 Finally, we used the organoids to define the intrinsic regulatory pathways mediating  
301 trophoblast invasion (**Fig. 3i-j**). As in their *in vivo* counterparts, NOTCH-activated TFs (*HEY1*,  
302 *FOXM1*, *IRF6* low) and NF- $\kappa$ B TFs (*NFKB2*, *BACH2*, *JDP2*, *ATF3*) are present in VCT-CCC.  
303 The appearance of EVTS with an invasive phenotype is accompanied by downregulation of  
304 the WNT pathway (*CSRNPI*, *AXIN2* low), and upregulation of TFs involved in invasion (*ELK3*-  
305 *GATA3* complex<sup>41</sup>), tumour suppressor genes (*ELF4*, *GRHL1*) and the hypoxia inducible  
306 *HIF1a* pathway (*HIF1A*, *ARNT*, *STAT3*). Overall, we find the major programmes of EVT  
307 differentiation are conserved *in vivo* and *in vitro*. The subtle transcriptomic differences we  
308 encounter *in vitro* are likely to relate to the absence of maternal tissues. In addition, the lack  
309 of eEVTS in our culture indicates maternal factors absent in our cultures are required to define  
310 their identity.  
311

### 312 Modulation of trophoblast invasion by maternal cells in the decidua and myometrium

313

314 We next integrated single-cell and single-nuclei transcriptomics data from 18 donors to study  
315 how decidual maternal cells affect trophoblast invasion (**Fig. 1d, Fig. 4a, Supplementary Fig.**  
316 **2e**). We leveraged our tool CellPhoneDB v4<sup>18</sup> to determine the ligand-receptor interactions  
317 that are enriched in the four decidual ME (**Fig. 1a, see Methods**). We first focused on  
318 interactions mediating trophoblast invasion (**Fig. 4b**). As previously described<sup>14</sup>, decidual  
319 natural killer cells (dNKs) interact with EVTS through multiple ligand-receptor pairs  
320 (*TGFBR1/2-TGFB*, *PVR-TIGIT*, *PVR-CD96*, *CCR1-CCL5*, *CSF1R-CSF1*). We find that the  
321 majority of these receptors are upregulated in EVT-2, close to the cytotrophoblast cell columns  
322 (**Fig. 4c**). In this location *CSF1-CSF1R* interaction is enriched as shown by high-resolution  
323 multiplexed single molecule fluorescent *in situ* hybridisation (smFISH) (**Fig. 4d**). *CSF1* is  
324 characteristic of dNK1<sup>14,50</sup> and has a role in inducing tumour invasion<sup>51</sup>. Decidual  
325 macrophages (dM1 and dM2) are also likely to affect trophoblast invasion through expression  
326 of the chemokine *CXCL16*, which is known to interact with *CXCR6* upregulated in EVT-2 (**Fig.**  
327 **4c**). In addition, EVTS-2 express high levels of the guidance receptor *PLXND1* while its  
328 cognate ligand, *SEMA4C*, is characteristic of dM1.  
329

330 The iEVTS invade as far as the inner third of the myometrium when they have fused into  
331 placental bed GCs<sup>52</sup>. GCs are probably no longer invasive because the receptors *CSF1R* and  
332 *PLXND1* are downregulated (**Fig. 4b**). In contrast, GCs upregulate adhesion molecules

333 (JAM2, *EFNB1*, *SEMA4C*) whose cognate receptors are expressed by other iEVTs (*JAM3*,  
334 *EPHB2*, *EPHB3*, *PLXNB2*) that could be involved in cellular adhesion prior to their fusion<sup>7</sup>  
335 (**Fig. 4c**). Uterine smooth muscle cells (uSMCs) in the myometrium uniquely express *EPHB1*  
336 and *EPHB4* which bind to *EFNB1* upregulated in the iEVTs and GCs, possibly explaining their  
337 tropism towards the myometrium. We validated the expression of *EFNB1* in the GCs by  
338 multiplexed smFISH (**Fig. 4e**). Altogether, we show a group of ligand/receptor pairs by which  
339 immune cells in the decidua may control invasion of EVTs and how these are downregulated  
340 in GCs.

341

### 342 Decidual-trophoblast interactions mediating arterial remodelling

343

344 Trophoblast arterial transformation during early pregnancy is crucial for pregnancy success.  
345 Initially, there is medial destruction by iEVTs with replacement by acellular fibrinoid  
346 material<sup>2,36,52</sup>. Subsequently, eEVTs form a plug in the artery and partially replace the  
347 endothelium. This leads to loss of elasticity and dilation of the arteries essential to reduce the  
348 resistance to blood flow<sup>52,53</sup>. Making use of CellPhoneDB v4<sup>18</sup>, spatial transcriptomics and  
349 high-resolution microscopy, we next investigated how iEVTs and eEVTs jointly coordinate this  
350 process.

351

352 We mapped the interactions between perivascular cells (PVs)<sup>14</sup> and iEVT. Expression of  
353 *EFNB1* by iEVTs could induce their tropism towards the arteries as only PVs express the  
354 cognate receptor, *EPHB6* (**Fig. 5a**, **Fig. 4e**). We also find iEVTs upregulate specific cell  
355 signalling molecules (*PTPRS*, *NTN4*) whose cognate receptors are uniquely present in PVs  
356 (*NTRK3*, *NTRK2*) (**Fig. 5a**). This family of neurotrophic tyrosine receptor kinases (NTRKs) has  
357 been associated with cellular survival in other contexts and these interactions are possibly  
358 involved in the appearance of 'fibrinoid change' in the arterial media due to death of PVs by  
359 iEVTs<sup>2,36,52,53</sup>. Using multiplexed smFISH, we validated the specific interaction between iEVTs  
360 (*HLA-G+*) expressing *PTPRS* and PVs (*MCAM+*) expressing *NTRK3* in the arteries (**Fig. 5b**).  
361

362 The eEVT plugs limit maternal blood entering the intervillous space at high pressure before 8-  
363 10 PCW after which the full haemochorionic circulation is established<sup>54</sup>. Our unbiased analyses  
364 of eEVTs allowed us to predict how the plugs are formed, revealing a specific ECM pattern  
365 that enables homotypic interactions. For example, *ITGB1* and *ITGA2* are expressed in eEVTs  
366 which together form the a2b1 complex that interacts with collagens specifically expressed by  
367 eEVTs (*COL6A1*, *COL19A1*, *COL26A1*, *COL21A1*) (**Fig. 5c**). In addition, eEVTs upregulate  
368 both ligands (*JAG1* and *JAG2*) and receptors (*NOTCH2*, *NOTCH3*) that may stimulate active  
369 NOTCH signalling (**Fig. 5c**). Using spatial transcriptomics, we visualised the presence of ECM  
370 components (e.g. *COL21A1-ITGA2*) and NOTCH interactions (e.g. *NOTCH2-JAG1*) in the  
371 arterial plug (**Fig. 5d**).  
372

373 Expression of chemokines and adhesion molecules could mediate interactions between  
374 eEVTs and the arterial wall. eEVTs upregulate *CCR3*, *EPHA1*, *CXCL12*, *ERBB4* whose  
375 ligands are expressed by endothelial (*EFNA1*, *EFNA5*) and immune (*CCL3*, *EFNA5*, *HBEGF*,  
376 *CXCR4*, *EREG*) cells. The unique expression of *CXCL12* by eEVTs was validated by smFISH  
377 (**Fig. 5e**). eEVTs also upregulate *FLT4*, the receptor for *VEGFC*, upregulated by endothelial  
378 cells, and the growth factor *PDGFC* upregulated by endothelial cells, immune and PVs.  
379

380 Altogether, by examining cell-cell interactions in the distinct trophoblast subsets, we map the  
381 cellular and molecular events mediating the transformation of the arteries during early  
382 pregnancy (**Fig. 5f**).

383

## 384 Discussion

385

386 In the post-implantation embryo, trophectoderm differentiates into trophoblast, the defining  
387 epithelial cells of the placenta that invade the uterus to transform the maternal arteries.  
388 Defective trophoblast invasion is the primary underlying cause of the great obstetric  
389 syndromes that include pre-eclampsia, fetal growth restriction, unexplained stillbirth, placental  
390 abruption and preterm labour<sup>4</sup>. We report new multiomics and spatial data, and develop a  
391 statistical framework (StOrder) that describes the complete trophoblast invasion trajectory  
392 during the first trimester of pregnancy. This includes the unbiased transcriptomics profile of  
393 eEVTs that move down inside the maternal arteries, and placental bed GCs, present deeper  
394 in the decidua and the inner myometrium.

395

396 We made use of a historical collection of pregnant hysterectomies at 8-10 PCW to delineate  
397 the landscape of the trophoblast at the implantation site, the place where fetal and maternal  
398 cells intermingle. The human implantation sites profiled in our study were collected more than  
399 30 years ago and have been stored in liquid nitrogen. The discovery that these historical  
400 samples are so well preserved that we could use them for cutting edge single-cell  
401 transcriptomic analysis is important. Such samples are rare today owing to advances in clinical  
402 treatments that avoid hysterectomy during pregnancy. More broadly it shows how unanswered  
403 biological questions can be answered using such old samples. Our experimental design that  
404 combined consecutive sections for spatial transcriptomics and single-cell multiomics methods  
405 allowed us to integrate the molecular and cellular profiles with their spatial coordinates.

406

407 We define the transcriptomic profile of a VCT subset that can commit into SCT via a VCT-  
408 fusing intermediate, or invading EVT<sup>s</sup> via VCT located in the column niche (VCT-CCC). All  
409 these VCT subsets are present in our tissue-derived trophoblast organoid model,  
410 demonstrating that both *in vivo* and *in vitro*, VCTs can give rise to both EVT<sup>s</sup> and SCT. This  
411 is in line with the observation that clonally derived trophoblast organoids can give rise to both  
412 cell types<sup>55</sup>. However, as VCT differentiate to EVT, there are subtle differences in the  
413 intermediate EVT subsets emerging *in vivo* and *in vitro*. Differences between *in vivo* and *in*  
414 *vitro* datasets could be explained by transient EVT populations not being captured in our *in*  
415 *vivo* dataset or because the influence of maternal serum and decidua tissues is lacking *in*  
416 *vitro*. Despite these small differences in the subsets emerging from the cytotrophoblast cell  
417 columns *in vivo* and *in vitro*, we do find an iEVT subset in the organoids that is present deeper  
418 in decidua *in vivo*. To compare this subset to *in vivo* iEVT<sup>s</sup>, we used the probabilistic method  
419 cell2location and can confirm that *in vitro*-iEVT<sup>s</sup> are equivalent to iEVT<sup>s</sup> present in ME3 from  
420 the *in vivo* spatial transcriptomics data. This means that our trophoblast organoid model can  
421 be used to explore questions such as how placental bed GCs form.

422

423 We developed StOrder, which uses both spatial and single-cell transcriptomics events to  
424 reconstruct the trajectory of trophoblast invasion and to identify bifurcation points. All code is  
425 available in our github and can be applied to other scenarios where lineage decisions are  
426 correlated with spatial changes. Our framework can be tailored to other spatial technologies  
427 by adapting specific parameters such as the distance between spots considered. StOrder

428 pointed to EVT-2, located at the tips of the villi (or outer part of the cytotrophoblast shell), as  
429 the most likely precursors of eEVTs. Our result is consistent with previous histological  
430 observations suggesting that eEVTs arise from the cell columns or shell and move down the  
431 arterial lumen<sup>35,36,56</sup>. Using an approach that considers both TF expression and activity, we  
432 found eEVT identity is marked by a strong upregulation of NOTCH and HIF1A and a  
433 downregulation of TGF $\beta$  signalling. eEVTs are not found in the *in vitro* organoid model. This  
434 could be due to the absence of maternal endothelial cells or serum, or the non-hypoxic culture  
435 conditions.

436

437 Our systems biology approach has also allowed us to explore how the arterial transformation  
438 by both iEVTs and eEVTs is coordinated. Histological studies show that the medical  
439 destruction (fibrinoid change) is seen after iEVTs have encircled the arteries and it is only after  
440 this that eEVTs form a plug and then move down the artery in a retrograde manner to partially  
441 replace the endothelium<sup>2,36,52</sup>. We find selective interactions between iEVTs and PVs that may  
442 drive their tropism towards the arterial wall and mediate the destruction of arterial smooth  
443 muscle media. On the other hand, eEVTs have a specific ECM that could allow them to form  
444 the plug. There are also specific interactions with endothelial cells allowing adherence of  
445 eEVTs to them. These novel interactions add to our understanding of the communication  
446 between endothelial and eEVT cells<sup>57</sup>. The impact of defective arterial transformation in the  
447 later stages of pregnancy is well-described and underpins the great obstetric syndromes<sup>6</sup>. Our  
448 study increases understanding of these major pregnancy disorders that all have their origins  
449 in the first trimester<sup>58</sup>.

450

451 Deep trophoblast invasion into the uterus is exclusive to human and great apes<sup>10</sup>, and pre-  
452 eclampsia is only observed in humans<sup>59</sup>. Until now, our understanding of trophoblast invasion  
453 deep into the myometrium *in vivo* has mainly been limited to morphological and histological  
454 studies of archival specimens. Our study has identified markers of trophoblast invasion during  
455 a healthy pregnancy that can be compared to pathological conditions and cross referenced in  
456 genetic studies. Parallels are observed in other biological scenarios, such as cancer or tissue  
457 regeneration, and thus, some of the fundamental processes described in this work may  
458 extrapolate to other contexts. In addition, our bioinformatics tools will have a broader use for  
459 inferring spatial ordering of cells in other contexts, such as the tumour microenvironment.  
460 Finally, our roadmap of trophoblast differentiation can be used as a blueprint to design  
461 improved *in vitro* models that fully recapitulate the early stages after implantation.

462

463

464

## 465 **Figure legends**

466

### 467 **Figure 1 Trophoblast cell states in the early maternal-fetal interface.**

468 **a:** Schematic representation of the maternal-fetal interface (MFI) in early human pregnancy in  
469 the first trimester (left) and overview of experimental design of the study (right).

470 **b:** Histological overview (H&E staining) of the implantation site of donor P13 (~ 8-9 post-  
471 conceptional weeks, PCW); black squares indicate trophoblast microenvironments in space.

472 **c:** High-resolution imaging of a section of the placenta-decidua interface stained by *in situ*  
473 hybridization (smFISH) for HLA-G, illustrating the depth of invasion of EVTs into the uterus.  
474 Magnified insets (dashed squares) highlight the HLA-G-negative placental villi, and HLA-G-  
475 positive EVTs emerging from the CCC to invade the decidua and myometrium.

476 **d:** Cohort composition split by gestational age (PCW) window representing tissues sampled  
477 from each donor and performed assays. Highlighted in red rectangles are the three donors  
478 whose tissues have been additionally profiled with spatial (Visium) and multiome assays.  
479 **e:** UMAP (uniform manifold approximation and projection) scatterplot of snRNA-seq of donor  
480 P13 trophoblast cell states in the maternal-fetal interface (n = 37,675 nuclei) coloured by cell  
481 state.  
482 **f:** Overview of spatial locations of invading trophoblast cell states in Visium spatial  
483 transcriptomics data of representative section of donor P13 (position of capture area is  
484 indicated with an arrow in Supplementary Fig. 1a). Cell type densities represented are derived  
485 with cell2location. Colorbars indicate the cell densities in a Visium spot. Invading trophoblast  
486 cell states are grouped based on the spatial microenvironment they represent.  
487 **g:** Dot plots show the variance-scaled, log-transformed expression of genes (X-axis)  
488 characteristic of trophoblast cell states (Y-axis) in donor P13 snRNA-seq data.  
489 **h:** Dot plot showing the variance-scaled, log-transformed expression of genes (X-axis)  
490 characteristic of villous cytotrophoblast (VCT) (Y-axis) in donor P13 snRNA-seq data.  
491 Syncytiotrophoblast (SCT), villous cytotrophoblast (VCT), cytotrophoblast cell column (CCC),  
492 proliferative (p), extravillous trophoblast (EVT), giant cells (GC), endovascular EVT (eEVT),  
493 single-cell RNA sequencing (scRNA-seq), single-nuclei RNA sequencing (snRNA-seq),  
494 microenvironment (ME).

495  
496 **Figure 2 Regulatory programmes mediating extravillous trophoblast invasion.**  
497 **a:** Schematic overview of StOrder approach representing the workflow of joint cell  
498 differentiation trajectory inference from gene expression and spatial data showing a  
499 representative tree with gene expression contribution of  $\omega = 0.4$ .  
500 **b:** UMAP (uniform manifold approximation and projection) scatterplot of multiome (snRNA-  
501 ATACseq) data of invading trophoblast from donor P13 (n = 829) coloured by cell state. The  
502 manifold is calculated based on dimensionality reduction performed by MEFISTO (based on  
503 n=9 factors).  
504 **c:** Percentage of variance explained by each MEFISTO factor in each data modality.  
505 **d:** UMAP scatterplots of multiome (snRNA-ATACseq) data of invading trophoblast from donor  
506 P13 (n = 1605) as in **b** coloured by cell cycle phase and MEFISTO factor values for important  
507 selected factors  
508 **e:** Heatmap showing z-score of normalised, log-transformed and scaled expression of  
509 transcription factors (TF) relevant for trophoblast invasion in all donors. Y-axis indicates cell  
510 state, X-axis lists TFs. Differential expression is tested along invading trophoblast trajectory  
511 (as shown in Fig.2a) in a retrograde manner. Annotations of TFs on top of the heatmap are  
512 encoded as follows: asterix (\*) = supported by MEFISTO; "a" = active TF.  
513 **f:** Dot plot showing the variance-scaled, log-transformed expression of genes (X-axis) of  
514 signalling molecules upregulated in EVT (Y-axis) in all donors.  
515 **g:** Schematic representation of signalling pathways in distinct microenvironments (see Figure  
516 1a).  
517 Villous cytotrophoblast (VCT), cytotrophoblast cell column (CCC), proliferative (p), extravillous  
518 trophoblast (EVT), giant cells (GC), endovascular EVT (eEVT), microenvironment (ME), gene  
519 expression (GEX).

520  
521 **Figure 3 Regulatory programmes in primary derived trophoblast organoids.**  
522 **a:** Schematic representation of the extravillous trophoblast differentiation experimental design,  
523 indicating time points and biological replicates (donors).

524 **b:** Phase-contrast images of trophoblast organoids plated in a Matrigel droplet and exposed  
525 to TOM or EVTM. Scale bar is 1 mm.  
526 **c:** UMAP (uniform manifold approximation and projection) scatterplot coloured by growth  
527 medium.  
528 **d:** (Left) Predicted trophoblast subsets of placental organoids using a logistic classifier trained  
529 on P13 data. (Right) Logistic regression probabilities.  
530 **e:** UMAP scatterplot with final annotations of trophoblast subsets.  
531 **f:** Dot plot showing the variance-scaled, log-transformed expression of genes (X-axis)  
532 characteristic of villous cytotrophoblast (VCT) (Y-axis) in placental organoids.  
533 **g:** Dot plots show the variance-scaled, log-transformed expression of genes (X-axis)  
534 characteristic of trophoblast cell states (Y-axis) in placental organoids.  
535 **h:** Spatial locations of iEVTs in Visium spatial transcriptomics data of representative Visium  
536 section of donor P13 (position of capture area is indicated with an arrow in Supplementary  
537 Fig. 1A). Cell type densities represented are derived with cell2location trained on single-cell  
538 transcriptomics data of trophoblast organoids. Colorbars indicate the cell densities in a Visium  
539 spot.  
540 **i:** Heatmap showing z-score of normalised, log-transformed and scaled expression of  
541 transcription factors (TF) relevant for trophoblast invasion. Y-axis indicates cell state, X-axis  
542 lists TFs. Differential expression is tested along invading trophoblast trajectory (as shown in  
543 Fig.2a) in a retrograde manner.  
544 **j:** Dot plot showing the variance-scaled, log-transformed expression of genes (X-axis) of  
545 signalling molecules upregulated in EVT (Y-axis) in trophoblast organoids.  
546 Syncytiotrophoblast (SCT), villous cytotrophoblast (VCT), cytotrophoblast cell column (CCC),  
547 proliferative (p), extravillous trophoblast (EVT), giant cells (GC), endovascular EVT (eEVT),  
548 single-cell RNA sequencing (scRNA-seq), single-nuclei RNA sequencing (snRNA-seq).  
549

550 **Figure 4 Cell-cell communication mediating extravillous trophoblast invasion.**  
551 **a:** UMAP (uniform manifold approximation and projection) scatterplot of scRNA-seq and  
552 snRNA-seq of all donors described in Fig. 1d in the maternal-fetal interface (n = 350 815 cells  
553 and nuclei) coloured by cell state  
554 **b:** (Left) Dot plot showing the variance-scaled, log-transformed expression of genes (X-axis)  
555 of selected receptors upregulated in VCT-CCC (Y-axis) in trophoblast from all donors. (Right)  
556 Dot plot showing the presence (X-axis) of selected ligands in cells present in ME 3 (invasion  
557 front). Differential expression is tested along invading trophoblast trajectory (as shown in Fig.  
558 2a) in a retrograde manner.  
559 **c:** (Left) Dot plot showing the variance-scaled, log-transformed expression of genes (X-axis)  
560 of selected receptors upregulated in EVT-1 and/or EVT-2 and or iEVT (Y-axis) in trophoblast  
561 from all donors. (Right) Dot plot showing the presence (X-axis) of selected ligands in cells  
562 present in ME 4 (decidual/myometrial border). Differential expression is tested along invading  
563 trophoblast trajectory (as shown in Fig. 2a) in a retrograde manner.  
564 **d:** (Left) High-resolution imaging of a section of the placenta-decidua interface stained by  
565 smFISH for *HLA-G*, highlighting EVTs invading the decidua from the CCC. (Centre)  
566 multiplexed co-staining with *NCAM1* (dNK marker), *CSF1* and cognate receptor *CSF1R*;  
567 dashed squares indicate areas shown magnified to right. (Right) solid and outlined arrows  
568 indicate neighbouring *CSF1R*-expressing EVTs and *CSF1*-expressing dNK cells, respectively.  
569 Representative image of samples from three donors.  
570 **e:** High-resolution imaging of a section of the placenta-decidua interface stained by  
571 multiplexed smFISH for *HLA-G* and *EFNB1*, demonstrating that expression of *EFNB1* is

572 present throughout EVTs, including iEVTs, and elevated in GCs. Small inset at bottom-centre  
573 illustrates the multinucleated nature of GCs. Representative image of samples from two  
574 donors.

575 Villous cytotrophoblast (VCT), cytotrophoblast cell column (CCC), extravillous trophoblast  
576 (EVT), giant cells (GC), endovascular EVT (eEVT).

577

578 **Figure 5 Cell-cell communication mediating arterial transformation during the first-  
579 trimester of pregnancy.**

580 **a:** (Left) Dot plot showing the variance-scaled, log-transformed expression of genes (X-axis)  
581 of selected receptors upregulated in iEVT(Y-axis) in trophoblast from all donors. (Right) Dot  
582 plot showing the presence (X-axis) of selected ligands in cells present in ME 3 (invasion front).  
583 Differential expression is tested along invading trophoblast trajectory (as shown in Fig. 2a) in  
584 a retrograde manner.

585 **b:** (Top) High-resolution imaging of a section of decidua stained by multiplexed smFISH for  
586 *HLA-G*, *MCAM* (PV marker), *NTRK3* and its receptor *PTPRS*; dashed squares indicate areas  
587 shown magnified underneath. (Middle and below) solid and outlined arrows indicate  
588 neighbouring *PTPRS*-expressing EVTs and *NTRK3*-expressing dNK cells, respectively.  
589 Representative image of samples from three donors.

590 **c:** (Left) Dot plot showing the variance-scaled, log-transformed expression of genes (X-axis)  
591 of selected receptors upregulated in VCT-CCC (Y-axis) in trophoblast from all donors. In the  
592 case of a complex, the expression corresponds to the least expressed subunit of the complex  
593 (*ITGB1*). (Right) Dot plot showing the presence (X-axis) of selected ligands in cells present in  
594 ME 5 (spiral arteries). Differential expression is tested along invading trophoblast trajectory  
595 (as shown in Fig. 2A) in a retrograde manner.

596 **d:** Overview of spatial locations of invading trophoblast cell states in Visium spatial  
597 transcriptomics data of representative section of donor P13 (position of capture area is  
598 indicated with an arrow in Supplementary Fig. 1a). Cell type densities represented are derived  
599 with cell2location. Colorbars indicate the cell densities in a Visium spot.

600 **e:** (Left) High-resolution imaging of a section of decidua stained by multiplexed smFISH for  
601 *HLA-G*, *NCAM1*, and *CXCL12*. Dashed squares highlight arteries containing *HLA-G*+

602 *NCAM1* eEVTs expressing *CXCL12*, shown magnified to right. Representative image of  
603 samples from two donors.

604 **f:** Schematic representation of the spiral arteries in early human pregnancy in the first trimester  
605 highlighting the novel interactions between PV-iEVT, endothelial-eEVT, immune-eEVT and  
606 eEVT-eEVT that we found in our dataset.

607 Villous cytotrophoblast (VCT), cytotrophoblast cell column (CCC), extravillous trophoblast  
608 (EVT), giant cells (GC), endovascular EVT (eEVT).

609

610

## 611 **Supplementary Material**

612

## 613 **Supplementary Figures**

614

### 615 **Supplementary Fig. 1 Spatial transcriptomics of the implantation site.**

616 **a:** Histological overview (H&E staining) of donors P13, P14 and Hrv43 tissues with annotations  
617 of tissue regions. For the implantation site of donor P13 (~ 8-9 post-conceptional weeks, PCW,  
618 left); black squares indicate trophoblast microenvironments in space; faint grey squares (big)

619 indicate positioning of tissue on Visium spatial transcriptomics capture areas; arrow indicates  
620 representative Visium section further explored in Fig. 1f.

621 **b:** Cell state locations (derived with cell2location) for representative Visium sections of donors  
622 P14 and Hrv43 highlighting relevant spatial trophoblast microenvironments.

623 Syncytiotrophoblast (SCT), villous cytotrophoblast (VCT), cytotrophoblast cell column (CCC),  
624 proliferative (p), extravillous trophoblast (EVT), giant cells (GC), endovascular EVT (eEVT),  
625 single-cell RNA sequencing (scRNA-seq), single-nuclei RNA sequencing (snRNA-seq),  
626 microenvironment (ME).

627

628 **Supplementary Fig. 2 Overview of analysis and quality control of coarse cell states in**  
629 **scRNA-seq and snRNA-seq data for the maternal-fetal interface.**

630 **a:** Overview of the computational pipeline implemented for analysis of scRNA-seq and snRNA-  
631 seq data.

632 **b-e:** (top) UMAP (uniform manifold approximation and projection) scatterplots of donors P13,  
633 P14, Hrv43 and all donors' data (b-e respectively) for all recovered cell states, colored by  
634 coarse grain compartment annotation and important metadata labels: assay, sample (10X  
635 library), donor and developmental age. (bottom) Dot plots show the variance-scaled, log-  
636 transformed expression of genes characteristic of coarse grain compartment (X-axis) in  
637 donors profiled (Y-axis).

638 Maternal (m), fetal (f), natural killer (NK), innate lymphocytes (ILC)

639

640 **Supplementary Fig. 3 Overview of quality control of trophoblast cell states in scRNA-**  
641 **seq and snRNA-seq data for the maternal-fetal interface.**

642 **a:** UMAP (uniform manifold approximation and projection) scatterplots of donor P13 snRNA-  
643 seq data for all trophoblast cell states colored by assay, sample (10X library) and cell cycle  
644 phase of the nuclei.

645 **b:** UMAP scatterplot of integrated snRNA-seq and scRNA-seq of all donors' trophoblast cell  
646 states in the maternal-fetal interface (n = 75,042 nuclei and cells) coloured by cell state

647 **c:** UMAP scatterplots of all donors' scRNA-seq and snRNA-seq data for all trophoblast cell  
648 states colored by assay, sample (10X library), cell cycle phase of the cells/nuclei, donor and  
649 developmental age

650 **d:** Dot plots show the variance-scaled, log-transformed expression of genes (X-axis)  
651 characteristic of trophoblast cell states (Y-axis) in all donors.

652 **e:** Dot plots show the variance-scaled, log-transformed expression of genes (X-axis)  
653 characteristic of trophoblast cell states (Y-axis) in all donors.

654 **f:** Results of PAGA trajectory inference of all trophoblast cell states in donor P13 snRNA-seq  
655 data (left: main manifold, center: denoised PAGA manifold, right: PAGA reconstruction of  
656 putative trajectory tree for all trophoblast cell states). For the purpose of this analysis all EVTs  
657 have been united in annotation under 'EVT' label.

658 Syncytiotrophoblast (SCT), villous cytotrophoblast (VCT), cytotrophoblast cell column (CCC),  
659 proliferative (p), extravillous trophoblast (EVT), giant cells (GC), endovascular EVT (eEVT),  
660 single-cell RNA sequencing (scRNA-seq), single-nuclei RNA sequencing (snRNA-seq).

661

662 **Supplementary Fig.4 Multimodal analysis of extravillous trophoblast invasion.**

663 **a:** (Left) Main UMAP (uniform manifold approximation and projection) scatterplot and (right)  
664 denoised manifold used for PAGA trajectory inference of all trophoblast cell states in donor  
665 P13 snRNA-seq data.

666 **b:** PAGA reconstruction of putative trajectory tree for all extravillous trophoblast cell states.  
667 This corresponds to the trajectory inferred using  $\omega = 1$  in StOrder.

668 **c:** Reconstruction of putative invading trophoblast trajectory tree based on both gene  
669 expression and spatial data (range of  $\omega \in [0.3, 0.48]$  in stOrder approach). stOrder was  
670 performed on donor P13 snRNA-seq and donors P13, P14 and Hrv43 spatial locations for  
671 invading trophoblast and VCT\_CCC cell states.

672 **d:** Reconstruction of putative invading trophoblast trajectory tree based solely on spatial data  
673 ( $\omega=0$  in stOrder approach). stOrder was performed on donor P13 snRNA-seq and donors P13,  
674 P14 and Hrv43 spatial locations for invading trophoblast and VCT\_CCC cell states.

675 **e:** Overview of the computational pipeline implemented for analysis of multimodal data.

676 **f:** UMAP scatterplots of integrated multimodal data from donors P13, P14 and hrv43. Data  
677 annotated based on the snRNA-seq annotation.

678 **g:** UMAP scatterplots coloured by donor, sample and unbiased clustering

679 **h:** UMAP scatterplots of trophoblast cell states.

680 **i:** (Left) UMAP scatterplot of multiome (snRNA-ATACseq) data of invading trophoblast from  
681 donor P13 ( $n = 829$ ) coloured by sample. The manifold is calculated based on dimensionality  
682 reduction performed by MEFISTO (model with  $n=9$  factors). (Right) Scatterplot of UMAP  
683 coordinates obtained from the RNA expression data that were used as covariates for  
684 MEFISTO. Each dot corresponds to a cell coloured by lineage assignment.

685 **j:** Estimated smoothness along differentiation.

686 **k:** Learnt correlation structure for each latent factor.

687 **l:** Gene set (RNA, left) enrichment analysis overview of MEFISTO factor 2.

688 **m:** Peak set (ATAC, right) enrichment analysis overview of MEFISTO factor 10.

689 Villous cytotrophoblast (VCT), cytotrophoblast cell column (CCC), proliferative (p), extravillous  
690 trophoblast (EVT), giant cells (GC), endovascular EVT (eEVT), dendritic cells (DC), lymphatic  
691 (l), maternal (M), Hofbauer cells (HOFB), innate lymphocytes (ILC), macrophages (M),  
692 monocytes (MO), natural killer (NK), perivascular (PV), decidua (d), epithelial (epi), stromal  
693 (S), fibroblasts (F), uterine smooth muscle cells (uSMC).

694

695 **Supplementary Fig. 5. NCAM1+ eEVTs emerging from the cytotrophoblast cell column**  
696 (Top) High-resolution imaging of sections of the placenta-decidua interface stained by  
697 multiplexed smFISH for *HLA-G* and *NCAM1*. (Middle) magnified insets highlight  
698 cytotrophoblast cell columns and solid arrows indicate *HLA-G*+ *NCAM1*+ cells (nascent  
699 eEVTs) shown magnified below (bottom). Images of samples from two donors shown.

700

701 **Supplementary Fig. 6. Benchmark of primary-derived placental organoids.**

702 **a:** UMAP (uniform manifold approximation and projection) scatterplots of 6 organoid donors  
703 colored by donor, time-point and cell cycle.

704 **b:** UMAP scatterplot coloured by unbiased clustering using louvain.

705 **c:** Dot plot showing the variance-scaled, log-transformed expression of genes (X-axis) of main  
706 trophoblast subsets (Y-axis) on each of the cells identified by unbiased clustering (B).

707 **d:** Bar plot showing the proportion of predicted cell states by our logistic regression model on  
708 each of the identified clusters (B).

709 **e:** Bar plot showing the proportion of final cell states identified on each donor (left) and time-  
710 point (right).

711 **f:** Overview of spatial locations of EVT-mid and iEVT subsets in 10X Visium spatial  
712 transcriptomics data in Visium sections of donor P13. Cell type densities represented are  
713 derived with cell2location with single-cell transcriptomics data from the organoids used as a  
714 reference. Colorbars indicate the cell state density in a Visium spot.

715 **g:** Scatterplot of cell densities derived by cell2location of *in vitro* iEVT (X-axis, using single-  
716 cell transcriptomics of trophoblast organoids) vs *in vivo* iEVT (Y-axis, using single-nucleus  
717 transcriptomics of donor P13) cell states in donor P13 Visium sections WS\_PLA\_S9101764,  
718 WS\_PLA\_S9101765, WS\_PLA\_S9101766 and WS\_PLA\_S9101767. In red is the trend line  
719 representing Spearman rank-order correlation ( $R = 0.91$ ,  $p$ -value  $< 10e-308$ , two-sided test)  
720 between values of cell densities of *in vivo* iEVT and *in vitro* iEVT. Syncytiotrophoblast (SCT),  
721 villous cytotrophoblast (VCT), cytotrophoblast cell column (CCC), proliferative (p), extravillous  
722 trophoblast (EVT), interstitial EVT (iEVT), giant cells (GC), endovascular EVT (eEVT).

723  
724

725 **Acknowledgements:** This publication is part of the Human Cell Atlas. We gratefully  
726 acknowledge the Sanger Cellular Generation and Phenotyping (CGaP) Core Facility and the  
727 Sanger Core Sequencing pipeline for support with sample processing and sequencing library  
728 preparation. Ricard Argelaguet for his help on MOFA/MEFISTO analysis. Vitalii  
729 Kleshchevnikov for this help on cell2location. Stijn van Dongen, Martin Prete and Simon  
730 Murray for their help on running pipelines and web portal support. Tarryn Porter for her help  
731 on preparing the libraries for spatial transcriptomics. Antonio Garcia for graphical images.  
732 Aidan Maartens for proofreading. Placental material was provided by the Joint MRC-Human  
733 Cell Atlas (MR/S036350/1). The authors are grateful to patients for donating tissue for  
734 research. We thank D. Moore and M. Maquinana and staff at Addenbrooke's Hospital,  
735 Cambridge, UK.

736 **Funding:** Supported by Wellcome Sanger core funding (WT206194) and the Wellcome Trust  
737 grant 'Wellcome Strategic Support Science award' (grant no. 211276/Z/18/Z). M.Y.T. held the  
738 Royal Society Dorothy Hodgkin Fellowship (DH160216) and Research Grant for Research  
739 Fellows (RGF\R1\180028) during this study and is also supported by funding from the  
740 European Research Council under the European Union's Horizon 2020 research and  
741 innovation programme (Grant agreement 853546).

742 **Contributions:** A.M collected and analysed the histology of the samples; E.P and R.H  
743 performed the nuclei experiments; K.R and E.T performed the spatial transcriptomics analyses  
744 with help of C.I.M and I.K; M.A.S derived all organoid lines, performed all organoid culturing  
745 and prepared all time-point collections; A.A, B.V, L.G-A and K-T analysed all the data; A.A  
746 and I.K developed StOrder; A.A, M.Y.T and R.V.T interpreted the data with contribution of  
747 A.M, M.A.S and K.R; R.V.T and O.S supervised the bioinformatics analyses; R.V.T and O.B  
748 supervised the *in vivo* and genomics work; M.Y.T supervised the *in vitro* work; R.V.T wrote  
749 the manuscript with contributions from K.R, A.M, M.A.S, and A.A; the final version of the  
750 manuscript has been approved by all the authors.

751 **Competing interests:** S.A.T. has received remunerations for consulting and Scientific  
752 Advisory Board work from Genentech, Biogen, Roche, and GlaxoSmithKline as well as  
753 Foresite Labs over the past 3 years.

754 **Data availability:** Datasets are being uploaded into EMBL-EBI ArrayExpress and can now be  
755 accessed at <https://www.reproductivecellatlas.org/mfi/>. All codes used for data analysis are  
756 available from <https://github.com/ventolab/MFI>

757  
758

759

760 **Supplementary Tables**

761

762 **Supplementary Table 1. Supplementary\_Table\_1.xlsx (separate file)**

763 **Metadata of samples.** **(A)** 10X scRNA-seq libraries from human donors. **(B)** 10X snRNA-seq  
764 libraries from human donors. **(C)** 10X cell-coupled snRNA/ATAC-seq (multiome) libraries from  
765 human donors. **(D)** 10X Visium spatial transcriptomics libraries from human donors. Sample id  
766 = 10x reaction; Donor = donor ID; Stage\_PCW = post-conceptional weeks; TP = type of  
767 pregnancy termination (Med: medical; Sur: surgical or Hys: hysterectomy)

768

769 **Supplementary Table 2. Supplementary\_Table\_2.xlsx (separate file)**

770 **Quality control of samples for each 10X RNA library in our maternal-fetal interface atlas.**

771 **(A)** Summary statistics from 10X Cell Ranger 3.0.2 for scRNA-seq samples. **(B)** Summary  
772 statistics from 10X Cell Ranger 3.0.2 for snRNA-seq samples. **(C)** Summary statistics from  
773 10X Cell Ranger ARC 1.0.1 for multiome samples. **(D)** Summary statistics from 10X Space  
774 Ranger 1.1.0 Visium spatial transcriptomics samples.

775

776 **Supplementary Table 3. Supplementary\_Table3.xlsx (separate file)**

777 **Annotation summary for each sample.** Number of cells/nuclei (droplets) per coarse cell  
778 state in scRNA-seq, snRNA-seq and multiome samples of donors P13, P14, Hrv43 and all  
779 donors dataset.

780

781 **Supplementary Table 4. Supplementary\_Table4.xlsx (separate file)**

782 Variance explained (R2 column) in the MEFISTO model by each factor in each modality (RNA  
783 or ATAC).

784

785 **Supplementary Table 5. Supplementary\_Table5.xlsx (separate file)**

786 TF analysis along trophoblast trajectory. Table containing the multiple TF measurements in  
787 the *in vivo* analysis used to prioritise TF relevant for trophoblast differentiation of all TFs **(A)**  
788 and selected TFs **(B)**. All tests are performed by comparing the newly emerged cell type  
789 against the pseudo-ancestor. Columns across table indicate: TF = transcription factor; cluster  
790 = cell type; regulation\_sign = whether up or downregulation is tested; Avg\_expr = average log-  
791 transformed normalised expression within the cell type; is\_DE\_limma = 'yes' if it is a  
792 differentially expressed TF (FDR < 0.05; limma); is\_DA\_dorothea = 'yes' if it is a differentially  
793 activated TF (FDR < 0.05; Wilcoxon test); is\_DA\_chromVar = 'yes' if the TF binding motifs  
794 are differentially accessible (FDR < 0.05; Wilcoxon test); is\_DA\_MEFISTO = 'yes' if the  
795 TF binding motifs are differentially accessible in the regions linked to MEFISTO factor (FDR <  
796 0.05; Wilcoxon test); if\_DA\_MEFISTO\_factor = MEFISTO factor associated; is\_DE\_and\_DA  
797 = 'yes' if the TF is differentially expressed and differentially activated according to any other  
798 measure.

799

800 **Supplementary Table 6. Supplementary\_Table6.xlsx (separate file)**

801 Cell2location cell density values of *in vitro* iEVTs (using single-cell transcriptomics of  
802 trophoblast organoids) and *in vivo* iEVTs (using single-nucleus transcriptomics of donor P13)  
803 cell states in donor P13 Visium sections WS\_PLA\_S9101764, WS\_PLA\_S9101765,  
804 WS\_PLA\_S9101766 and WS\_PLA\_S910176.

805

806 **Supplementary Table 7. Supplementary\_Table7.xlsx (separate file)**

807 Trophoblast interactions enriched by microenvironment (ME) using CellPhoneDB. **(A)** ME2 =  
808 cytotrophoblast cell column. **(B)** ME3 = Invasion front. **(C)** ME4 = Decidual/myometrial border.  
809 **(D)** ME5 = Spiral arteries.  
810

811 **Supplementary Table 8. Supplementary\_Table8.xlsx (separate file)**

812 Probes used for multiplexed RNAscope smFISH.  
813

814 **Materials and methods**

815 **Patient samples**

816 Tissue samples used for this study were obtained with written informed consent from all  
817 participants in accordance with the guidelines in The Declaration of Helsinki 2000.  
818

819 Placental and decidual samples used for the *in vivo* and *in vitro* profiling were obtained from  
820 elective terminations from:

- 821 - The MRC and Wellcome-funded Human Developmental Biology Resource (HDBR,  
822 <http://www.hdbi.org>), with appropriate maternal written consent and approval from the  
823 Fulham Research Ethics Committee (REC reference 18/LO/0822) and Newcastle &  
824 North Tyneside 1 Research Ethics Committee (REC reference 18/NE/0290). The  
825 HDBR is regulated by the UK Human Tissue Authority (HTA; [www.hta.gov.uk](http://www.hta.gov.uk)) and  
826 operates in accordance with the relevant HTA Codes of Practice.
- 827 - Addenbrooke's Hospital (Cambridge) under ethical approval from the Cambridge Local  
828 Research Ethics Committee (04/Q0108/23), which is incorporated into The  
829 overarching ethics permission given to the Centre for Trophoblast Research biobank  
830 for the "Biology of the Human Uterus in Pregnancy and Disease Tissue Bank" at the  
831 University of Cambridge under ethical approval from the East of England-Cambridge  
832 Central Research Ethics Committee (17/EE/0151) and from the London-Hampstead  
833 Research Ethics Committee (20/LO/0115).

834

835 Placental/decidual blocks (P13, P14 and P34) were collected prior to 1 September 2006 and  
836 consent for research use was not obtained. These samples are considered 'Existing Holdings'  
837 under the Human Tissue Act and as such were able to be used in this project.  
838

839

840 All samples profiled were histologically normal.

841 **Tissue cryopreservation**

842 Fresh tissue samples of human implantation sites were embedded in cold OCT medium and  
843 flash frozen using a dry ice-isopentane slurry. Protocol available at [protocols.io<sup>60</sup>](https://protocols.io/60).

844 Quality of archival frozen tissue samples was assessed by extraction of RNA from  
845 cryosections using the QIAGEN RNeasy Mini Kit, according to the manufacturer's instructions

846 including on-column DNase I digestion. RNA quality was assayed using the Agilent RNA 6000  
847 Nano Kit. All samples processed for Visium and single-nuclei had RIN values greater than 8.7.

#### 848 Single-nuclei extraction

849 Single-nuclei suspensions were isolated from frozen tissue sections when performing  
850 multiomic snRNA-seq/scATAC-seq and snRNA-seq, following manufacturer's instructions.  
851 For each OCT-embedded sample, 400  $\mu$ m of tissue was prepared as 50  $\mu$ m cryosections,  
852 which were paused in a tube on dry ice until subsequent processing. Nuclei were released via  
853 Dounce homogenisation as described in detail at protocols.io<sup>61</sup>.

#### 854 Tissue processing

855 We used the previous protocol optimised for the decidua-placental interface<sup>14</sup>. In short,  
856 decidua tissues were enzymatically digested in 15 ml 0.4 mg/ml collagenase V (Sigma, C-  
857 9263) solution in RPMI 1640 medium (Thermo Fisher Scientific, 21875-034)/10% FCS  
858 (Biosfera, FB-1001) at 37 °C for 45 min. The supernatant was diluted with medium and passed  
859 through a 100- $\mu$ m cell sieve (Corning, 431752) and then a 40- $\mu$ m cell sieve (Corning, 431750).  
860 The flow-through was centrifuged and resuspended in 5 ml of red blood cell lysis buffer  
861 (Invitrogen, 00-4300) for 10 min. Placental villi were scraped from the chorionic membrane  
862 using a scalpel and the stripped membrane was discarded. The resultant villous tissue was  
863 enzymatically digested in 70 ml 0.2% trypsin 250 (Pan Biotech P10-025100P)/0.02% EDTA  
864 (Sigma E9884) in PBS with stirring at 37 °C for 9 min. The disaggregated cell suspension was  
865 diluted with medium and passed through a 100- $\mu$ m cell sieve (Corning, 431752). The  
866 undigested gelatinous tissue remnant was retrieved from the gauze and further digested with  
867 10–15 ml collagenase V at 1.0 mg/ml (Sigma C9263) in Ham's F12 medium/10% FBS with  
868 gentle shaking at 37 °C for 10 min. The disaggregated cell suspension was diluted with  
869 medium and passed through a 100- $\mu$ m cell sieve (Corning, 431752). Cells obtained from both  
870 enzyme digests were pooled together and passed through a 100- $\mu$ m cell sieve (Corning,  
871 431752) and washed in Ham's F12. The flow-through was centrifuged and resuspended in 5  
872 ml of red blood cell lysis buffer (Invitrogen, 00-4300) for 10 min.

#### 873 Trophoblast organoid cultures

874 In total, six trophoblast organoids were grown and differentiated into EVT as previously  
875 described<sup>11,55</sup>. To differentiate trophoblast organoids into EVT, organoids were cultured with  
876 trophoblast organoid media (TOM) for ~3-4 days and transferred into EVT media 1 (+NRG1)  
877 for ~4-7 days. Once trophoblasts initiate their commitment into EVT (spike emergence), EVT  
878 media 2 (-NRG1) is added for 4 days. Donors were differentiated and collected in batches of  
879 three that were multiplexed on the same 10x-genomics reaction. Samples for donors 1, 2 and  
880 3 were collected at 3 hours (h), 24h and 48h after addition of EVTM media 2, while samples  
881 for donors 4, 5 and 6 were collected at 48h before, and then 0h, 48h and 96h after, addition  
882 of EVTM media 2. Organoids grown in trophoblast organoid media (TOM) media were also  
883 collected as a control at 96h.

884

885 Media composition was as described previously<sup>11,55</sup>:

886 TOM = Advanced DMEM/F12, N2 supplement (at manufacturer's recommended  
887 concentration), B27 supplement minus vitamin A (at manufacturer's recommended  
888 concentration), Primocin 100 µg/mL, N-Acetyl-L-cysteine 1.25 mM, L-glutamine 2 mM,  
889 recombinant human EGF 50 ng/mL, CHIR99021 1.5 µM, recombinant human R-spondin-1 80  
890 ng/mL, recombinant human FGF-2 100 ng/mL, recombinant human HGF 50 ng/mL, A83-01  
891 500 nM, prostaglandin E2 2.5 µM, Y-27632 5 µM.

892

893 EVT media 1 = Advanced DMEM/F12, L-glutamine 2 mM, 2-mercaptoethanol 0.1 mM,  
894 penicillin/streptomycin solution 0.5% (vol/vol), BSA 0.3% (vol/vol), ITS-X supplement 1%  
895 (vol/vol), NRG1 100 ng/mL, A83-01 7.5 µM, Knockout serum replacement 4% (vol/vol)

896

897 EVT media 2 = Advanced DMEM/F12, L-glutamine 2 mM, 2-mercaptoethanol 0.1 mM,  
898 penicillin/streptomycin solution 0.5% (vol/vol), BSA 0.3% (vol/vol), ITS-X supplement 1%  
899 (vol/vol), A83-01 7.5 µM, Knockout serum replacement 4% (vol/vol) ie: EVT medium cat. no.  
900 1 without NRG1. Store the medium at 4°C for up to 1 week.

## 901 Haematoxylin and eosin (H&E) staining and imaging

902 Fresh frozen sections were removed from -80°C storage and air dried before being fixed in  
903 10% neutral buffered formalin for 5 minutes. After rinsing with deionised water, slides were  
904 stained in Mayer's haematoxylin solution for 90 seconds. Slides were completely rinsed in 4-  
905 5 washes of deionised water, which also served to blue the haematoxylin. Aqueous eosin (1%)  
906 was manually applied onto sections with a pipette and rinsed with deionised water after 1-3  
907 seconds. Slides were dehydrated through an ethanol series (70%, 70%, 100%, 100%) and  
908 cleared twice in 100% xylene. Slides were coverslipped and allowed to air dry before being  
909 imaged on a Hamamatsu Nanozoomer 2.0HT digital slide scanner.

## 910 Multiplexed smFISH and high-resolution imaging

911 Large tissue section staining and fluorescent imaging was conducted largely as described  
912 previously<sup>62</sup>. Sections were cut from fresh frozen samples embedded in OCT at a thickness  
913 of 10-16 µm using a cryostat, placed onto SuperFrost Plus slides (VWR) and stored at -80°C  
914 until stained. Tissue sections were processed using a Leica BOND RX to automate staining  
915 with the RNAscope Multiplex Fluorescent Reagent Kit v2 Assay (Advanced Cell Diagnostics,  
916 Bio-Techne), according to the manufacturers' instructions. Probes may be found in  
917 Supplementary Table 8. Prior to staining, fresh frozen sections were post-fixed in 4%  
918 paraformaldehyde in PBS for 6-8 hours, then dehydrated through a series of 50%, 70%, 100%,  
919 and 100% ethanol, for 5 minutes each. Following manual pre-treatment, automated  
920 processing included heat-induced epitope retrieval at 95°C for 15 minutes in buffer ER2 and  
921 digestion with Protease III for 15 minutes prior to probe hybridisation. Tyramide signal  
922 amplification with Opal 520, Opal 570, and Opal 650 (Akoya Biosciences) and TSA-biotin (TSA  
923 Plus Biotin Kit, Perkin Elmer) and streptavidin-conjugated Atto 425 (Sigma Aldrich) was used  
924 to develop RNAscope probe channels.

925 Stained sections were imaged with a Perkin Elmer Opera Phenix Plus High-Content Screening  
926 System, in confocal mode with 1 µm z-step size, using a 20X (NA 0.16, 0.299 µm/pixel) or  
927 40X (NA 1.1, 0.149 µm/pixel) water-immersion objective. Channels: DAPI (excitation 375 nm,  
928 emission 435-480 nm), Atto 425 (ex. 425 nm, em. 463-501 nm), Opal 520 (ex. 488 nm, em.

929 500-550 nm), Opal 570 (ex. 561 nm, em. 570-630 nm), Opal 650 (ex. 640 nm, em. 650-760  
930 nm).

931 Image stitching

932 Confocal image stacks were stitched as two-dimensional maximum intensity projections using  
933 proprietary Acapella scripts provided by Perkin Elmer.

934 10x Genomics Chromium GEX library preparation and sequencing

935 For the scRNA-seq experiments, cells were loaded according to the manufacturer's protocol  
936 for the Chromium Single Cell 3' Kit v3.0, v3.1 and 5' v1.0 (10X Genomics). Library preparation  
937 was carried out according to the manufacturer's protocol to attain between 2,000 and 10,000  
938 cells per reaction. Libraries were sequenced, aiming at a minimum coverage of 20,000 raw  
939 reads per cell, on the Illumina HiSeq 4000 or Novaseq 6000 systems; using the sequencing  
940 format;

- 941 a) read 1: 26 cycles; i7 index: 8 cycles, i5 index: 0 cycles; read 2: 98 cycles
- 942 b) read 1: 28 cycles; i7 index: 8 cycles, i5 index: 0 cycles; read 2: 91 cycles
- 943 c) read 1: 28 cycles; i7 index: 10 cycles; i5 index: 10 cycles; read 2: 90 cycles (v3.1 dual)

944  
945 For the multimodal snRNA-seq/scATAC-seq experiments, cells were loaded according to the  
946 manufacturer's protocol for the Chromium Single Cell Multiome ATAC + Gene Expression v1.0  
947 to attain between 2,000 and 10,000 cells per well. Library preparation was carried out  
948 according to the manufacturer's protocol. Libraries for scATAC-seq were sequenced on  
949 Illumina NovaSeq 6000, aiming at a minimum coverage of 10,000 fragments per cell, with the  
950 following sequencing format; read 1: 50 cycles; i7 index: 8 cycles, i5 index: 16 cycles; read 2:  
951 50 cycles.

952 10x Genomics Visium library preparation and sequencing

953 Ten micron cryosections were cut and placed on Visium slides, then processed according to  
954 the manufacturer's instructions. Briefly, sections were fixed with cold methanol, stained with  
955 haematoxylin and eosin and imaged on a Hamamatsu NanoZoomer S60 before  
956 permeabilisation, reverse transcription and cDNA synthesis using a template-switching  
957 protocol. Second-strand cDNA was liberated from the slide and single-indexed libraries  
958 prepared using a 10x Genomics PCR-based protocol. Libraries were sequenced (1 per lane  
959 on a HiSeq4000), aiming for 300M raw reads per sample, with the following sequencing  
960 format; read 1: 28 cycles, i7 index: 8 cycles, i5 index: 0 cycles and read 2: 91 cycles.

961 Alignment and quantification of scRNA-seq and snRNA-seq data

962 For each sequenced single-cell and single-nucleus RNA-seq library, we performed read  
963 alignment to the 10X Genomics' GRCh38 3.0.0 human reference genome, mRNA version for  
964 scRNA-seq samples and pre-mRNA version for snRNA-seq samples, latter created following  
965 instructions from 10X Genomics: <https://support.10xgenomics.com/single-cell-gene-expression/software/pipelines/latest/advanced/references#premra>. Quantification and initial  
966 quality control (QC) were performed using the Cell Ranger Software (version 3.0.2; 10X  
967

968 Genomics) using default parameters. Cell Ranger filtered count matrices were used for  
969 downstream analysis.

970 Alignment and quantification of multiome data

971 For each sequenced snRNA-ATAC-seq (multiome) library, we performed read alignment to  
972 custom made genome consisting of 10X Genomics' GRCh38 3.0.0 pre-mRNA human  
973 reference genome and 10X Genomics Cell Ranger-Arc 1.0.1 ATAC genome, created following  
974 instructions from 10X Genomics: <https://support.10xgenomics.com/single-cell-multiome-atac-gex/software/pipelines/latest/advanced/references>. Quantification and initial quality control  
975 (QC) were performed using the Cell Ranger-Arc Software (version 1.0.1; 10X Genomics) using  
976 default parameters. Cell Ranger-Arc filtered count matrices were used for downstream  
977 analysis.

979 Downstream scRNA-seq and snRNA-seq analysis

980 Detection of doublets by gene expression

981 We used Scrublet for cell doublet calling on a per-library basis. We used a two-step diffusion  
982 doublet identification followed by Bonferroni-FDR correction and a significance threshold of  
983 0.01, as described in<sup>63</sup>. Predicted doublets were not excluded from the initial analysis, but  
984 used afterwards to flag clusters with high doublet scores.

985

986 Detection of doublets by genotype

987 Souporcell<sup>64</sup> was used to deconvolute (a) maternal and fetal origin of cells and nuclei in our  
988 scRNA-seq and snRNA-seq samples (including multiome snRNA-seq); (b) assignment of cells  
989 to individuals in pooled samples (namely, samples Pla\_HDBR8768477, Pla\_HDBR8715512  
990 and Pla\_HDBR8715514); and (c) organoids from multiple individuals. In some samples  
991 deconvolution into maternal or fetal origin by genotype was not possible which is likely due to  
992 the highly skewed ratio of genotypes (either extremely high (>0.95) or extremely low (<0.05)  
993 ratio of maternal to fetal droplets). In those cases, maternal-fetal origin of the cells was  
994 identified using known markers from<sup>14</sup>.

995

996 Souporcell (version 2.4.0) was installed as per instructions in  
997 <https://github.com/wheaton5/souporcell> and used in the following way:

998 path\_to/singularity exec ./souporcell.sif souporcell\_pipeline.py -i

999 ./cellranger\_path/possorted\_genome\_bam.bam -b

1000 ./cellranger\_path/filtered\_feature\_bc\_matrix/barcodes.tsv -f ./genome\_path/genome.fa -t 8 -o

1001 souporcell\_result -k 2 --skip\_remap True --common\_variants

1002 ./filtered\_2p\_1kgenomes\_GRCh38.vcf

1003 Where k=2 corresponds to the number of individuals to be deconvoluted (in our case either  
1004 mother and fetus or pooled individuals H7 and H9 in samples Pla\_HDBR8768477,  
1005 Pla\_HDBR8715512 and Pla\_HDBR8715514. Accuracy of deconvolution was evaluated in  
1006 downstream analysis once cluster identity was clear from either gene expression or  
1007 predictions of logistic regression. In samples where deconvolution worked successfully,  
1008 inter-individual doublets were further excluded from downstream analysis.

1009 Filtering genes high in ambient RNA signal

1010 To assess which genes in the scRNA-seq and snRNA-seq data were high in ambient RNA  
1011 (soup) signal (further referred to as noisy genes), the following approach was undertaken  
1012 separately for all the scRNA-seq and snRNA-seq samples:

- 1013 1) Read in all the raw and filtered count matrices for each sample produced by Cell  
1014 Ranger Software
- 1015 2) Discard droplets with < 5 UMIs (likely to be fake droplets from sequencing errors)
- 1016 3) Only keep data from samples which we further consider as noisy (where “Fraction  
1017 reads in cells” reported by Cell Ranger is less than 70% (guided by 10X Genomics’  
1018 recommendations:  
1019 [https://assets.ctfassets.net/an68im79xiti/163qWiQBTVi2YLbskJphQX/e90bb82151b1cdab6d7e9b6c845e6130/CG000329\\_TechnicalNote\\_InterpretingCellRangerWebSummaryFiles\\_RevA.pdf](https://assets.ctfassets.net/an68im79xiti/163qWiQBTVi2YLbskJphQX/e90bb82151b1cdab6d7e9b6c845e6130/CG000329_TechnicalNote_InterpretingCellRangerWebSummaryFiles_RevA.pdf))
- 1020 4) Take the droplets that are in raw but are not in filtered matrices considering them as  
1021 empty droplets
- 1022 5) Concatenate all raw objects with empty droplets into 1 joint raw object and do the  
1023 same for filtered
- 1024 6) For all genes calculate soup probability as defined with the following equation:

$$1028 P = E_g^{\text{empty droplets}} / (E_g^{\text{empty droplets}} + E_g^{\text{cells/nuclei}}),$$

1029 Where  $E_g^{\text{empty droplets}}$  is the total sum of expression (number of UMI counts) of  
1030 gene g in empty droplets, and  $E_g^{\text{cells/nuclei}}$  is the total sum of expression counts of  
1031 gene g in droplets that are considered as cells/nuclei by Cell Ranger.

- 1032 7) For all genes calculate number of cells/nuclei where the gene is detected at >0  
1033 expression level (UMI counts)
- 1034 8) Label genes as noisy if their soup probability exceeds 50% quantile of soup  
1035 probability distribution - done separately for cells and for nuclei

1036  
1037 This approach was used to estimate noisy genes in (a) donor P13 samples and (b) all  
1038 donors’ samples. Donor P13 noisy genes were excluded during mapping onto space  
1039 (Visium, see section “Location of cell types in Visium data” below), whereas all donors’ noisy  
1040 genes (labelled using nuclei-only derived threshold in step 8 to not over-filter genes based  
1041 on the higher quality portion of the data which in our case in scRNA-seq) were excluded  
1042 during all donors analysis of the whole atlas of all the cell states at the maternal-fetal  
1043 interface.

1044 Quality filters, alignment of data across different batches, and clustering

1045 We integrated the filtered count matrices from Cell Ranger and analysed them with scanpy  
1046 (version 1.7.1), with the pipeline following their recommended standard practises. Briefly, we  
1047 excluded genes expressed by less than three cells, excluded cells expressing fewer than 200  
1048 genes, and cells with more than 20% mitochondrial content. After converting the expression  
1049 space to  $\log(\text{CPM}/100 + 1)$ , the object was transposed to gene space to identify cell cycling  
1050 genes in a data-driven manner, as described in <sup>63,65</sup>. After performing PCA, neighbour  
1051 identification and louvain clustering, the members of the gene cluster including known cycling  
1052 genes (*CDK1*, *MKI67*, *CCNB2* and *PCNA*) were flagged as the data-derived cell cycling  
1053 genes, and discarded in each downstream analysis where applicable.

1054 Next, to have an estimate of the optimal number of latent variables to be used later in the  
1055 single-cell Variational Inference (scVI) workflow for dimensionality reduction and batch  
1056 correction, we identified highly variable genes, scaled the data and calculated PCA to observe  
1057 the variance ratio plot and decide on an elbow point which defined values of n\_latent  
1058 parameter which were then used to correct for batch effect by 10X library batch ("sample")  
1059 with scVI. Number of layers in scVI models was tuned manually to allow for better integration.  
1060 The resulting latent representation of the data was used for calculating neighbourhood graph,  
1061 Uniform Manifold Approximation and Projection (UMAP) and further doing Louvain clustering.  
1062 Analysis was done separately for (a) donor P13 trophoblast compartment and (b) all donors'  
1063 data (all cell states). In both analyses (a) and (b) trophoblast data was analysed separately  
1064 with consecutive rounds of re-analysis upon exclusion of clusters of noisy nature (exhibiting  
1065 gene expression characteristic of more than 1 distinct population). In addition, in all donors'  
1066 analysis fibroblast (maternal and fetal separately) and maternal NK, T, myeloid, epithelial,  
1067 endothelial and perivascular compartments were re-analysed separately using the approach  
1068 described in the previous paragraph to achieve fine grain annotation.

1069 Differential gene expression analysis

1070 Differential gene expression analysis was performed with limma (limma version 3.46.0, edgeR  
1071 version 3.32.1) with "cell\_or\_nucleus" covariate (scRNA-seq or snRNA-seq (including  
1072 multiome snRNA-seq) origin of each droplet) backwards along the trajectory that was derived  
1073 using stOrder approach, namely for the following 6 comparisons: VCT\_CCC vs VCT (VCT and  
1074 VCT-p cell states together); EVT-1 vs VCT\_CCC; EVT-2 vs EVT-1; iEVT vs EVT-2; GC vs  
1075 iEVT; eEVT vs EVT-2.  
1076

1077 Alignment, quantification, and quality control of multiome ATAC data

1078 We processed scATAC-seq libraries coming from multiome samples (read filtering, alignment,  
1079 barcode counting, and cell calling) with 10X Genomics Cell Ranger-Arc (version 1.0.1) using  
1080 the pre-built 10X's GRCh38 genome (version corresponding to Cellranger-arc 1.0.1) as  
1081 reference. We called the peaks using an in-house implementation of the approach described  
1082 in Cusanovich et al.<sup>66</sup> (available at <https://github.com/cellgeni/cellatac>, revision 21-099). In  
1083 short, the genome was broken into 5 kb windows and then each cell barcode was scored for  
1084 insertions in each window, generating a binary matrix of windows by cells. Matrices from all  
1085 samples were concatenated into a unified matrix, which was filtered to retain only the top 200K  
1086 most commonly used windows per sample. Using Signac (<https://satijalab.org/signac/> version  
1087 0.2.5), the binary matrix was normalised with term frequency-inverse document frequency (TF-  
1088 IDF) followed by a dimensionality reduction step using Singular Value Decomposition (SVD).  
1089 The first latent semantic indexing (LSI) component was ignored as it usually correlates with  
1090 sequencing depth (technical variation) rather than a biological variation<sup>66</sup>. The 2-30 top  
1091 remaining components were used to perform graph-based Louvain clustering. Next, peaks  
1092 were called separately on each cluster using macs2<sup>67</sup>. Finally, peaks from all clusters were  
1093 merged into a master peak set (i.e. peaks overlapping in at least one base pair were  
1094 aggregated) and used to generate a binary peak by cell-matrix, indicating any reads occurring  
1095 in each peak for each cell.

1096 This analysis was done separately for (a) all multiome data at first and (b) trophoblast only  
1097 subset of the multiome data. In the latter analysis we used annotation labels from the RNA  
1098 counterpart of the multiome samples to perform peak calling.

1099 Alignment, quantification, and quality control of Visium data

1100 For each 10X Genomics Visium sample, we used Space Ranger Software Suite (version  
1101 1.1.0) to align to the GRCh38 human reference pre-mRNA genome (official Cell Ranger  
1102 reference, version 3.0.0) and quantify gene counts. Spots were automatically aligned to the  
1103 paired H&E images by Space Ranger software. All spots under tissue detected by Space  
1104 Ranger were included in downstream analysis.

1105 Downstream analysis of 10X Genomics Visium data

1106 Location of cell types in Visium data

1107 To locate the cell states in the Visium transcriptomics slides, we used the cell2location tool  
1108 v0.06-alpha<sup>68</sup>. As reference, we used snRNA-seq data of donor P13. We used general cell  
1109 state annotations from the joint all donors' analysis (corresponding to donor P13 data), with  
1110 the exception of the trophoblast lineage. Trophoblast annotations were taken from donor P13-  
1111 only analysis of the trophoblast compartment. Using information about which genes are noisy  
1112 (high in ambient RNA signal) in donor P13 snRNA-seq data (please see details in "Filtering  
1113 genes high in ambient RNA signal" section above), we excluded those from the reference and  
1114 Visium objects prior to cell2location model training which significantly improved the results of  
1115 mapping (namely, eliminated off-target mapping of cell states, i. e. made results of mapping  
1116 more specific to the correct anatomical regions). Following the tutorial:  
1117 [https://cell2location.readthedocs.io/en/latest/notebooks/cell2location\\_tutorial.html#Cell2location-on-spatial-mapping](https://cell2location.readthedocs.io/en/latest/notebooks/cell2location_tutorial.html#Cell2location-on-spatial-mapping), we trained cell2location model with default parameters using 10X library  
1118 as a batch covariate in the step of estimation of reference cell type signatures. Results were  
1119 visualised with scanpy (version 1.7.1). Plots represent estimated abundance of cell types (cell  
1120 densities) in Visium spots.

1122 Subsetting Visium data into anatomical regions with SpatialDE2

1123 We used SpatialDE2<sup>69</sup> tissue segmentation algorithm to assign Visium spots to three  
1124 anatomical regions: (a) placenta; (b) decidua\_and\_villi\_tips and (c) myometrium. We used  
1125 mRNA abundances from the deconvolution results obtained with cell2location<sup>24</sup> in SpatialDE2  
1126 tissue segmentation. Assignment of obtained Visium spot clusters to regions was done upon  
1127 visual inspection. Locations of certain fibroblast cell states indicative of the specific anatomical  
1128 region (uterine smooth muscle cells, uSMC, and decidual stromal cells ,dS, cell states) were  
1129 also used to guide this assignment. In addition, low quality spots were discarded based on i)  
1130 not being under tissue and, ii) having low count and gene coverage (visual inspection).  
1131 For more details, please refer to the following notebook:  
1132 [https://github.com/ventolab/MFI/blob/main/2\\_inv\\_troph\\_trajectory\\_and\\_TFs/2-1\\_stOrder\\_inv\\_troph/S1\\_regions\\_analysis\\_for\\_SpCov\\_model\\_and\\_later\\_for\\_CellPhone.ipynb](https://github.com/ventolab/MFI/blob/main/2_inv_troph_trajectory_and_TFs/2-1_stOrder_inv_troph/S1_regions_analysis_for_SpCov_model_and_later_for_CellPhone.ipynb)

1135 Downstream snATAC-seq analysis

1136 Quality filters

1137 To obtain a set of high quality peaks for downstream analysis, we filtered out peaks that (i)  
1138 were included in the ENCODE blacklist, (ii) have a width outside the 210-1500bp range and  
1139 (iii) were accessible in less than 5% of cells from a *cellatac* cluster. Low quality cells were also  
1140 removed by setting to 4 the minimum threshold for log1p transformed total counts per cell.

1141

1142 Alignment of data across different batches and clustering

1143 We adopted the *cisTopic* approach<sup>70,71</sup> for the core of our downstream analysis. *cisTopic*  
1144 employs Latent Dirichlet Allocation (LDA) to estimate the probability of a region belonging to  
1145 a regulatory topic (region-topic distribution) and the contribution of a topic within each cell  
1146 (topic-cell distribution). The topic-cell matrix was used for constructing the neighbourhood  
1147 graph, computing UMAP projections and clustering with the Louvain algorithm. After this was  
1148 done for all cell states, clusters corresponding to trophoblast cell states (based on the  
1149 unbiased clustering done here and annotation labels coming from the RNA counterpart of this  
1150 multiome data) were further subsetted and re-analysed following the same pipeline.

1151

1152 Gene activity scores

1153 Next, we generated a denoised accessibility matrix (predictive distribution) by multiplying the  
1154 topic-cell and region-topic distribution and used it to calculate gene activity scores. To be able  
1155 to integrate them with sc/snRNA-seq data, gene activity scores were rounded and multiplied  
1156 by a factor of 10<sup>7</sup>, as previously described<sup>71</sup>.

1157

1158 Cell type annotation of invading trophoblast

1159 Final labels of invading trophoblast in snATAC-seq data were directly transferred from RNA  
1160 counterpart of the multiome data.

1161 StOrder: join inference of trophoblast invasion from gene expression and spatial  
1162 data

1163

1164 StOrder is a computational framework for joint inference of cellular differentiation trajectories  
1165 from gene expression data and information about location of cell states in physical space  
1166 (further referred to as spatial data).

1167

1168 It consists of three principal steps:

1169

- 1170 1. Calculate pairwise cell state connectivity from gene expression data (here we use  
1171 snRNA-seq data).
- 1172 2. Calculate pairwise cell state proximity in physical space from spatial data (here we use  
1173 Visium spatial transcriptomics data) using a new spatial covariance model.
- 1174 3. Combine connectivity matrices from steps 1 and 2 in a weighted sum to reconstruct  
1175 the putative tree structure of the differentiation trajectory.

1176

1177 First, StOrder relies on a gene expression-based connectivity matrix (generated in our case  
1178 by PAGA<sup>72</sup>) that establishes potential connections between cell state clusters defined by  
1179 single cell/nucleus transcriptomics datasets. The values in this matrix can be interpreted as

1180 pairwise similarity scores for cell states in gene expression space. In our case we used  
1181 snRNA-seq data from P13 as it contains all trophoblast subsets.  
1182

1183 Second, StOrder generates a spatial covariance matrix that reflects pairwise proximity of cell  
1184 states that co-exist in space and smoothly transition from one state to another while physically  
1185 migrating in space. To do so, StOrder takes as an input the deconvolution results (derived in  
1186 our case with cell2location<sup>24</sup>) of Visium spatial transcriptomics data. Here, we used all spatial  
1187 transcriptomics data profiled (donors P13, P14 and Hrv43). Then, it fits a Gaussian Process  
1188 (GP) model that derives pairwise spatial covariance scores for all the cell state pairs with the  
1189 following model:

$$\text{vec}(\mathbf{Y}_i \mathbf{Y}_j) \sim \mathcal{N} \left( \mathbf{0}, \begin{pmatrix} \sigma_1^{(1)} & \sigma_2^{(1)} \\ \sigma_2^{(1)} & \sigma_3^{(1)} \end{pmatrix} \otimes K(\mathbf{X}, l) + \begin{pmatrix} \sigma_1^{(2)} & 0 \\ 0 & \sigma_2^{(2)} \end{pmatrix} \otimes \mathbf{I} \right)$$

1190  
1191  
1192

1193 where  $\otimes$  is the Kronecker product and the combined vector of cell densities  $(\mathbf{Y}_{i,k} \mathbf{Y}_{j,k})$  of cell  
1194 states  $i$  and  $j$  is modelled by a multivariate Gaussian distribution whose covariance  
1195 decomposes into a spatial and a noise term. The spatial term

$$\begin{pmatrix} \sigma_1^{(1)} & \sigma_2^{(1)} \\ \sigma_2^{(1)} & \sigma_3^{(1)} \end{pmatrix} \otimes K(\mathbf{X}, l)$$

1196 is defined by a between-cell-state covariance matrix

$$\begin{pmatrix} \sigma_1^{(1)} & \sigma_2^{(1)} \\ \sigma_2^{(1)} & \sigma_3^{(1)} \end{pmatrix}$$

1197  
1198

1199 1200 and a spatial covariance matrix  $K(\mathbf{X}, l)$  defined using the squared exponential kernel:

$$K(\mathbf{X}, l)_{mn} = \exp \left( -\frac{\|\mathbf{x}_m - \mathbf{x}_n\|^2}{2l^2} \right)$$

1201

1202  $\mathbf{x}_m$  and  $\mathbf{x}_n$  are spatial coordinates of spots m and n and l is the length scale of the smooth GP  
1203 function in space that is being fit to cell densities.

1204 The noise term

$$\begin{pmatrix} \sigma_1^{(2)} & 0 \\ 0 & \sigma_2^{(2)} \end{pmatrix} \otimes \mathbf{I}$$

1205  
1206

1207 represents sources of variation other than spatial covariance of cell state densities.  
1208 The between-cell-state covariance matrix is constrained to be symmetric positive definite by  
1209 defining

$$\begin{pmatrix} \sigma_1^{(1)} & \sigma_2^{(1)} \\ \sigma_2^{(1)} & \sigma_3^{(1)} \end{pmatrix} = \begin{pmatrix} a_1 & 0 \\ a_2 & a_3 \end{pmatrix} \begin{pmatrix} a_1 & 0 \\ a_2 & a_3 \end{pmatrix}^T$$

1210

1211 The free parameters  $a_1$ ,  $a_2$ ,  $a_3$ ,  $\sigma_1^{(2)}$ ,  $\sigma_2^{(2)}$ , and l are estimated using maximum likelihood and  
1212 automatic differentiation in Tensorflow<sup>73,74</sup> using the BFGS algorithm. To improve  
1213 convergence, we initialise l to the distance between centres of neighboring Visium spots.

1214  
1215 This model allows us to infer which cell states are proximal in physical space and are likely to  
1216 be migrating in the process of gradual differentiation in space.  
1217  
1218 For the spatial covariance model within StOrder workflow we only used a subset of our Visium  
1219 data that corresponded to (a) decidua\_and\_villi\_tips and (b) myometrium - because only these  
1220 regions contained invading trophoblast cell states. For more details please see section  
1221 "Subsetting Visium data into anatomical regions with SpatialDE2" in "Downstream analysis of  
1222 10x Genomics Visium data" above. This helps to focus on the regions of the tissue that are  
1223 relevant for the process of interest and is recommended to do in general if there are parts of  
1224 the Visium data that do not contain cell states relevant to the process of interest.  
1225  
1226 Third, StOrder reconstructs connections between cell states by taking into account both the  
1227 connectivity matrix (step 1) from single-cell transcriptomics data and the spatial covariance  
1228 matrix (step 2) from the spatial data by summing the two matrices in a weighted manner and  
1229 reconstructing the putative trajectory tree using the built-in PAGA functions.  
1230  
1231 The combined connectivity matrix based on both gene expression and spatial data with a  
1232 range of weight parameters ( $0.16 \leq \omega \leq 0.47$  for gene expression weight/contribution) revealed  
1233 the fully resolved invasion trajectory tree of the EVT with the correct topology (all connected  
1234 cell state components, one branching point, no cycles, start at VCT-CCC population and two  
1235 endpoints: eEVT and GC populations). The choice of  $\omega$  parameter (contribution/weight of gene  
1236 expression vs spatial part in the final matrix) in this last step depends on the goal of using this  
1237 approach. In our case, we assumed: (i) the origin of EVT (VCT-CCC) ; (ii) the endpoints of  
1238 EVT (eEVT and GC); (iii) the determination of a single branching point; and (iv) the absence  
1239 of cyclic trajectory. We therefore produced trajectory trees for 101 values of  $\omega$  parameter (from  
1240 0 to 1 with 0.01 increment step) representative of different tree topologies corresponding to  
1241 different ratios of gene expression vs spatial contribution. Out of the 101 tree structures we  
1242 inspected for  $\omega$  values in the  $[0.16, 0.47]$  interval the trees represented the topology with the  
1243 assumptions described above. These trajectories consistently assigned EVT-2 as the putative  
1244 branching point. Tree structures for  $\omega > 0.47$  (mainly gene expression based connectivities)  
1245 values did not yield a branching point population we were looking for. Tree structures with  $\omega$   
1246  $< 0.16$  (mainly spatial based connectivities) hindered the link between iEVT and GC  
1247 populations, likely due to the large length scale of this invasion in space.  
1248  
1249 Limitations: Our approach assumes the gradual nature of gene expression changes  
1250 accompanied by gradual migration of cells in space while they differentiate. Thus, it may not  
1251 yield meaningful results in scenarios where this underlying assumption is violated. In addition,  
1252 it is recommended that the user estimates the spatial scale at which the process of interest is  
1253 taking place - whether in current Visium resolution the differentiation and migration is

1254 happening over the course of only a few spots or many more - this will change the initial values  
1255 of  $\lambda$  parameter and help the model fit the data better.

## 1256 Combined RNA/ATAC analysis using MEFISTO

### 1257 Preprocessing of multiome data and training of the MEFISTO model

1258 Gene expression (snRNA-seq) counts of the multiome data for donor P13 were normalised by  
1259 total counts (scipy.stats.normalize\_per\_cell(rna, counts\_per\_cell\_after=1e4)) and log  
1260 transformed (np.log1p(rna)). Highly variable gene features were then calculated  
1261 (sc.stats.highly\_variable\_genes(rna, min\_mean=0.0125, max\_mean=3, min\_disp=0.5)) and the  
1262 subsetted object's expression was scaled (sc.stats.scale(rna, max\_value=10)).

1263

1264 Chromatin accessibility (scATAC-seq) counts of the multiome data for donor P13 were  
1265 preprocessed using TF-IDF normalisation (muon.atac.stats.tfidf(atac[key], scale\_factor=1e4)).  
1266 To select biologically meaningful highly variable peak features, ATAC counts were aggregated  
1267 into pseudobulks by cell states and averaged, then variance of accessibility was calculated  
1268 across these pseudobulks, and informative peak features were selected based on this  
1269 measure (top 75th percentile (10640) of peaks selected in total) as the peaks with highest  
1270 variance. Lastly, this data was scaled (sc.stats.scale(atac, max\_value=10)).

1271

1272 Using the preprocessed RNA and ATAC data we used a pseudotime-aware dimensionality  
1273 reduction method MEFISTO<sup>37</sup> to extract major sources of variation from the RNA and ATAC  
1274 data jointly and identify coordinated patterns along the invasion trajectory. As a proxy for the  
1275 trophoblast invasion trajectory in the MEFISTO model we used 2-dimensional pseudotime  
1276 coordinates based on a UMAP of the RNA data by calculating PCA (sc.tl.pca(rna,  
1277 n\_comps=8)), neighborhood graph (sc.stats.neighbors(rna)) and UMAP embedding  
1278 (sc.tl.umap(rna)).

1279

1280 The MEFISTO model was trained using the following command within MUON (version 0.1.2)  
1281 package interface:

```
1282 muon.tl.mofa(mdata, outfile=",
1283     use_obs = "union",
1284     smooth_covariate=["UMAP1", "UMAP2"],
1285     use_float32=True)
```

1286

1287 We further excluded factor 5 from downstream analysis as a technical artefact due to its  
1288 significant and high correlation (Spearman rank-order correlation coefficient 0.94 (over all cell  
1289 states), p-value < 10e-308, two-sided test) with the n\_peaks\_by\_counts (number of ATAC  
1290 peaks with at least 1 count in a nucleus) in ATAC view in all cell states (**Supp. Fig. 4k**) and  
1291 lack of smoothness along pseudotime (**Supp. Fig. 4j**).

1292

### 1293 Defining groups of ATAC peak features

1294 To further interpret ATAC features, we annotated them based on their genomic location using  
1295 GenomicRanges package (version 1.42.0). In parallel, we used epigenetic data from<sup>75</sup> to mark  
1296 peak features in close proximity to trophoblast-specific enhancer features. To do so, we used  
1297 peak files corresponding to H3K4me1, H3K27ac and H3K27me3 histone modifications marks  
1298 for second trimester trophoblast samples (obtained from authors of aforementioned study  
1299 upon request) to infer regions of the genome corresponding to active (H3K27ac + H3K27me3),

1300 primed (only H3K4me1) or repressed (H3K4me1 + H3K27me3) enhancers. This was done  
1301 using bedtools (version 2.30.0) in the following way:

- 1302 1) bedtools subtract -a H3K4me1\_file.bed -b H3K27ac\_file.bed > interm\_file.bed
- 1303 bedtools subtract -a interm\_file.bed -b H3K27me3\_file.bed > primed\_enhancers.bed
- 1304 To produce primed enhancers file
- 1305 2) bedtools intersect -a H3K4me1\_file.bed -b H3K27ac\_file.bed > active\_enhancers.bed
- 1306 To produce active enhancers file
- 1307 3) bedtools intersect -a H3K4me1\_file.bed -b H3K27me3\_file.bed > repressed\_enhancers.bed
- 1308 To produce repressed enhancers file

1310

1311 The enhancer files produced were then overlapped with peaks in ATAC analysis (bedtools  
1312 intersect -a atac\_peaks\_file.bed -b enhancer\_file.bed -wa) and any peaks having a >1bp  
1313 overlap with an enhancer feature were considered to be proximal to those features (done  
1314 separately for active, primed and repressed enhancers).

1315

#### 1316 Enrichment analysis of features in the MEFISTO model

1317 Gene set enrichment analysis for gene features was performed based on the C5 category and  
1318 the Biological Process subcategory from the MSigDB database (<https://www.gsea-msigdb.org/gsea/msigdb>) using GSEA functionality implemented in MOFA2 (run\_enrichment  
1319 command, MOFA2 version 1.3.5). This was done separately for negative and positive weights  
1320 of each factor.

1321 Peak group enrichment for peak features was performed using the same run\_enrichment  
1322 command in MOFA2 on peak groups defined as described above (Defining groups of ATAC  
1323 peak features).

1324

#### 1325 TF analysis using the MEFISTO model

1326 To extract information about TF binding motif enrichment in ATAC features of MEFISTO  
1327 factors, we first performed enrichment analysis of peaks using GSEA functionality  
1328 implemented in MOFA2 (run\_enrichment command, MOFA2 version 1.3.5) on the peak-motif  
1329 matrix produced by Signac package (version 1.5.0). Then, to identify which MEFISTO factors  
1330 contribute the most to each transition of cell states along the invading trophoblast trajectory  
1331 (inferred with StOrder), we trained logistic regression classifiers for each transition along the  
1332 trajectory (overall for 6 transitions: VCT → VCT-CCC, VCT-CCC → EVT-1, EVT-1 → EVT-2,  
1333 EVT-2 → iEVT, iEVT → GC, EVT-2 → eEVT) on the matrix of factor values. For each transition  
1334 the factor with the highest absolute coefficient separating the two cell states was selected,  
1335 accounting for the sign of contribution in the logistic regression (positive or negative). If the  
1336 top factor is contributing to a transition with a positive coefficient, TF binding motifs coming  
1337 from MEFISTO enrichment analysis of this factor's top positive values are further considered  
1338 in general TF analysis as TFs upregulated upon this transition, whereas TF binding motifs

1340 coming from MEFISTO enrichment analysis of this factor's top negative values are further  
1341 considered in general TF analysis as TFs downregulated upon this transition. All of these TF  
1342 motifs are marked as having evidence from the MEFISTO factor relevant for this transition.  
1343 Reverse procedure is applied in case if the top factor is contributing to a transition with a  
1344 negative coefficient in the corresponding logistic regression model.

1345 For more details please see the following notebook:  
1346 [https://github.com/ventolab/MFI/blob/main/2\\_inv\\_troph\\_trajectory\\_and\\_TFs/2-5\\_MEFISTO\\_analysis\\_inv\\_troph/S3\\_DEG\\_comparison\\_to\\_MEFISTO\\_factor\\_translation.ipynb](https://github.com/ventolab/MFI/blob/main/2_inv_troph_trajectory_and_TFs/2-5_MEFISTO_analysis_inv_troph/S3_DEG_comparison_to_MEFISTO_factor_translation.ipynb)  
1347  
1348  
1349

## 1350 CellPhoneDB and CellSign

1351 To retrieve interactions between invading trophoblast and other cell populations identified in  
1352 our samples, we used CellPhoneDB v4 'degs\_analysis' method <sup>14, 76</sup>  
1353 (<https://github.com/ventolab/CellphoneDB>) described in <sup>23</sup>. In short, we retrieved the  
1354 interacting pairs of ligands and receptors meeting the following requirements: 1) all the protein  
1355 members were expressed in at least 10% of the cell type under consideration; and 2) at least  
1356 one of the protein members in the ligand or the receptor was a differentially expressed gene  
1357 in an invading trophoblast subset (according to our analysis of differential expression, for  
1358 details please see section "Differential gene expression analysis" above), with an adjusted p-  
1359 value below 0.05. We further selected which cell states are spatially co-located in each  
1360 microenvironment via visual inspection of cell2location deconvolution results for our Visium  
1361 data.

## 1362 Transcription Factor (TF) analysis

1363 To prioritise the TFs relevant for each invading trophoblast cell state or microenvironment, we  
1364 integrate four types of measurements: (i) expression levels of the TF and (ii) the activity status  
1365 of the TF measured from (ii-a) the expression levels of their targets (described below in  
1366 "*Transcription factor activities derived from scRNA-seq and snRNA-seq*") and/or (ii-b) the  
1367 chromatin accessibility of their binding motifs (described below in "*Transcription factor motif*  
1368 *activity analysis from scATACseq*") and/or (ii-c) evidence of the chromatin accessibility of their  
1369 binding motifs in relevant factors from multimodal RNA-ATAC analysis (with MEFISTO). Plots  
1370 in main figures include TF meeting the following criteria: 1) TF was differentially expressed,  
1371 with adjusted p-value < 0.01, and/or 2) TF was differentially active, with log2 fold change  
1372 greater than 0.75 and adjusted p-value < 0.01 in at least one of the TF activity measurements  
1373 (iiia/iiib).

1374

1375 Transcription factor differential expression (from scRNAseq and snRNA-seq)

1376 We compute differential expression using the procedure described in section "Differential gene  
1377 expression analysis" above and further subset resulting gene targets to TFs only based on the  
1378 list of TFs provided by DoRothEA.

1379

1380 Transcription factor activities derived from scRNAseq and snRNAseq

1381 We estimated protein-level activity for human Transcription factors (TF) as a proxy of the  
1382 combined expression levels of their targets. Target genes were retrieved from *Dorothea*<sup>77</sup>, an  
1383 orthogonal collection of TF targets compiled from a range of different sources. Next, we  
1384 estimated TF activities for each cell using *Viper*<sup>78</sup>, a GSEA-like approach, as implemented in  
1385 the *Dorothea* R package and tutorial<sup>79</sup> for the genes differentially expressed along the  
1386 invading trophoblast trajectory (see section “Differential gene expression analysis” above).

1387

1388 Transcription factor motif activity analysis from scATACseq

1389 Transcription factor motif activities were computed using chromVar<sup>80</sup> v. 1.12.2 with positional  
1390 weight matrices from JASPAR2018<sup>81</sup>, HOCOMOCOv10<sup>82</sup>, SwissRegulon<sup>83</sup>, HOMER<sup>84</sup>.  
1391 chromVar returns a matrix with binding activity estimates of each TF in each cell, which we  
1392 used to test for differential TF binding activity between trophoblast cell states with FindMarkers  
1393 function in Seurat (default parameters) in the same way as described in section “Differential  
1394 gene expression analysis” above (backwards along invading trophoblast trajectory).

1395

1396

1397

1398 **References**

- 1399 1. Turco, M. Y. & Moffett, A. Development of the human placenta. *Development* **146**, (2019).
- 1400 2. Pijnenborg, R., Vercruyse, L. & Hanssens, M. The uterine spiral arteries in human  
1401 pregnancy: facts and controversies. *Placenta* **27**, 939–958 (2006).
- 1402 3. Burton, G. J. & Jauniaux, E. The cytotrophoblastic shell and complications of pregnancy.  
*Placenta* **60**, 134–139 (2017).
- 1403 4. Brosens, I., Pijnenborg, R., Vercruyse, L. & Romero, R. The ‘Great Obstetrical  
1404 Syndromes’ are associated with disorders of deep placentation. *Am. J. Obstet. Gynecol.*  
1405 **204**, 193–201 (2011).
- 1406 5. Jauniaux, E. et al. Onset of maternal arterial blood flow and placental oxidative stress. A  
1407 possible factor in human early pregnancy failure. *Am. J. Pathol.* **157**, 2111–2122 (2000).
- 1408 6. Burton, G. J., Woods, A. W., Jauniaux, E. & Kingdom, J. C. P. Rheological and  
1409 physiological consequences of conversion of the maternal spiral arteries for  
1410 uteroplacental blood flow during human pregnancy. *Placenta* **30**, 473–482 (2009).
- 1411 7. al-Lamki, R. S., Skepper, J. N. & Burton, G. J. Are human placental bed giant cells merely  
1412 aggregates of small mononuclear trophoblast cells? An ultrastructural and  
1413 immunocytochemical study. *Hum. Reprod.* **14**, 496–504 (1999).
- 1414 8. Garrido-Gomez, T. et al. Defective decidualization during and after severe preeclampsia

1416 reveals a possible maternal contribution to the etiology. *Proc. Natl. Acad. Sci. U. S. A.*  
1417 **114**, E8468–E8477 (2017).

1418 9. Jauniaux, E. & Jurkovic, D. Placenta accreta: pathogenesis of a 20th century iatrogenic  
1419 uterine disease. *Placenta* **33**, 244–251 (2012).

1420 10. Carter, A. M., Enders, A. C. & Pijnenborg, R. The role of invasive trophoblast in  
1421 implantation and placentation of primates. *Philos. Trans. R. Soc. Lond. B Biol. Sci.* **370**,  
1422 20140070 (2015).

1423 11. Turco, M. Y. *et al.* Trophoblast organoids as a model for maternal-fetal interactions during  
1424 human placentation. *Nature* **564**, 263–267 (2018).

1425 12. Haider, S. *et al.* Self-Renewing Trophoblast Organoids Recapitulate the Developmental  
1426 Program of the Early Human Placenta. *Stem Cell Reports* **11**, 537–551 (2018).

1427 13. Sheridan, M. A. *et al.* Characterization of primary models of human trophoblast.  
1428 *Development* **148**, (2021).

1429 14. Vento-Tormo, R. *et al.* Single-cell reconstruction of the early maternal-fetal interface in  
1430 humans. *Nature* **563**, 347–353 (2018).

1431 15. Suryawanshi, H. *et al.* A single-cell survey of the human first-trimester placenta and  
1432 decidua. *Science Advances* **4**, eaau4788 (2018).

1433 16. Fawkner-Corbett, D. *et al.* Spatiotemporal analysis of human intestinal development at  
1434 single-cell resolution. *Cell* **184**, 810–826.e23 (2021).

1435 17. Asp, M. *et al.* A Spatiotemporal Organ-Wide Gene Expression and Cell Atlas of the  
1436 Developing Human Heart. *Cell* **179**, 1647–1660.e19 (2019).

1437 18. Garcia-Alonso, L. *et al.* Single-cell roadmap of human gonadal development. *Preprint*  
1438 from Research Square (2021) doi:10.21203/rs.3.rs-496470/v1 .

1439 19. Haniffa, M. *et al.* A roadmap for the Human Developmental Cell Atlas. *Nature* **597**, 196–  
1440 205 (2021).

1441 20. Moncada, R. *et al.* Integrating microarray-based spatial transcriptomics and single-cell  
1442 RNA-seq reveals tissue architecture in pancreatic ductal adenocarcinomas. *Nat.*  
1443 *Biotechnol.* (2020) doi:10.1038/s41587-019-0392-8.

1444 21. Maniatis, S. *et al.* Spatiotemporal dynamics of molecular pathology in amyotrophic lateral  
1445 sclerosis. *Science* **364**, 89–93 (2019).

1446 22. He, Z. *et al.* Lineage recording reveals dynamics of cerebral organoid regionalization.  
1447 *bioRxiv* 2020.06.19.162032 (2020) doi:10.1101/2020.06.19.162032.

1448 23. Garcia-Alonso, L. *et al.* Mapping the temporal and spatial dynamics of the human  
1449 endometrium in vivo and in vitro. *Cold Spring Harbor Laboratory* 2021.01.02.425073  
1450 (2021) doi:10.1101/2021.01.02.425073.

1451 24. Kleshchevnikov, V. *et al.* Cell2location maps fine-grained cell types in spatial  
1452 transcriptomics. *Nat. Biotechnol.* (2022) doi:10.1038/s41587-021-01139-4.

1453 25. Shannon, M. J. *et al.* Cell trajectory modeling identifies a primitive trophoblast state  
1454 defined by BCAM enrichment. *Development* **149**, (2022).

1455 26. Wolf, F. A. *et al.* PAGA: graph abstraction reconciles clustering with trajectory inference  
1456 through a topology preserving map of single cells. *Genome Biology* vol. 20 (2019).

1457 27. Mi, S. *et al.* Syncytin is a captive retroviral envelope protein involved in human placental  
1458 morphogenesis. *Nature* **403**, 785–789 (2000).

1459 28. Haider, S. *et al.* Notch1 controls development of the extravillous trophoblast lineage in  
1460 the human placenta. *Proc. Natl. Acad. Sci. U. S. A.* **113**, E7710–E7719 (2016).

1461 29. Lee, C. Q. E. *et al.* Integrin  $\alpha$ 2 marks a niche of trophoblast progenitor cells in first  
1462 trimester human placenta. *Development* **145**, (2018).

1463 30. Shen, L. *et al.* Lysophosphatidylcholine acyltransferase 1 promotes epithelial-  
1464 mesenchymal transition of hepatocellular carcinoma via the Wnt/ $\beta$ -catenin signaling  
1465 pathway. *Ann. Hepatol.* **27**, 100680 (2022).

1466 31. Chang, W.-L. *et al.* PLAC8, a new marker for human interstitial extravillous trophoblast  
1467 cells, promotes their invasion and migration. *Development* **145**, (2018).

1468 32. Vasyutina, E., Martarelli, B., Brakebusch, C., Wende, H. & Birchmeier, C. The small G-  
1469 proteins Rac1 and Cdc42 are essential for myoblast fusion in the mouse. *Proc. Natl.*  
1470 *Acad. Sci. U. S. A.* **106**, 8935–8940 (2009).

1471 33. Charrin, S. *et al.* Normal muscle regeneration requires tight control of muscle cell fusion

1472 by tetraspanins CD9 and CD81. *Nat. Commun.* **4**, 1674 (2013).

1473 34. Gaccioli, F., Aye, I. L. M. H., Sovio, U., Charnock-Jones, D. S. & Smith, G. C. S.

1474 Screening for fetal growth restriction using fetal biometry combined with maternal

1475 biomarkers. *Am. J. Obstet. Gynecol.* **218**, S725–S737 (2018).

1476 35. Burrows, T. D., King, A. & Loke, Y. W. Expression of adhesion molecules by

1477 endovascular trophoblast and decidual endothelial cells: Implications for vascular

1478 invasion during implantation. *Placenta* **15**, 21–33 (1994).

1479 36. Kam, E. P., Gardner, L., Loke, Y. W. & King, A. The role of trophoblast in the physiological

1480 change in decidual spiral arteries. *Hum. Reprod.* **14**, 2131–2138 (1999).

1481 37. Velten, B. *et al.* Identifying temporal and spatial patterns of variation from multimodal data

1482 using MEFISTO. *Nat. Methods* **19**, 179–186 (2022).

1483 38. Jokhi, P. P., King, A., Sharkey, A. M., Smith, S. K. & Loke, Y. W. Screening for cytokine

1484 messenger ribonucleic acids in purified human decidual lymphocyte populations by the

1485 reverse-transcriptase polymerase chain reaction. *J. Immunol.* **153**, 4427–4435 (1994).

1486 39. Apps, R. *et al.* Genome-wide expression profile of first trimester villous and extravillous

1487 human trophoblast cells. *Placenta* **32**, 33–43 (2011).

1488 40. Nguyen, B.-C. *et al.* Cross-regulation between Notch and p63 in keratinocyte

1489 commitment to differentiation. *Genes Dev.* **20**, 1028–1042 (2006).

1490 41. Kong, S.-Y. *et al.* The ELK3-GATA3 axis orchestrates invasion and metastasis of breast

1491 cancer cells in vitro and in vivo. *Oncotarget* **7**, 65137–65146 (2016).

1492 42. Burton, G. J., Cindrova-Davies, T., Yung, H. W. & Jauniaux, E. HYPOXIA AND

1493 REPRODUCTIVE HEALTH: Oxygen and development of the human placenta.

1494 *Reproduction* **161**, F53–F65 (2021).

1495 43. Yi, T., Papadopoulos, E., Hagner, P. R. & Wagner, G. Hypoxia-inducible factor-1α (HIF-

1496 1α) promotes cap-dependent translation of selective mRNAs through up-regulating

1497 initiation factor eIF4E1 in breast cancer cells under hypoxia conditions. *J. Biol. Chem.*

1498 **288**, 18732–18742 (2013).

1499 44. Froese, N. *et al.* GATA6 promotes angiogenic function and survival in endothelial cells

1500 by suppression of autocrine transforming growth factor beta/activin receptor-like kinase  
1501 5 signaling. *J. Biol. Chem.* **286**, 5680–5690 (2011).

1502 45. Wang, J. *et al.* HMGA2 contributes to vascular development and sprouting angiogenesis  
1503 by promoting IGFBP2 production. *Exp. Cell Res.* **408**, 112831 (2021).

1504 46. Chaves-Moreira, D. *et al.* PAX8 orchestrates an angiogenic program through interaction  
1505 with SOX17. *bioRxiv* 2020.09.09.290387 (2020) doi:10.1101/2020.09.09.290387.

1506 47. Liu, Y., Ao, X., Zhou, X., Du, C. & Kuang, S. The regulation of PBXs and their emerging  
1507 role in cancer. *J. Cell. Mol. Med.* **26**, 1363–1379 (2022).

1508 48. Starks, R. R. *et al.* Transcription Factor PLAGL1 Is Associated with Angiogenic Gene  
1509 Expression in the Placenta. *Int. J. Mol. Sci.* **21**, (2020).

1510 49. Okae, H. *et al.* Derivation of Human Trophoblast Stem Cells. *Cell Stem Cell* **22**, 50–63.e6  
1511 (2018).

1512 50. Jokhi, P. P., Chumbley, G., King, A., Gardner, L. & Loke, Y. W. Expression of the colony  
1513 stimulating factor-1 receptor (c-fms product) by cells at the human uteroplacental  
1514 interface. *Lab. Invest.* **68**, 308–320 (1993).

1515 51. Patsialou, A. *et al.* Autocrine CSF1R signaling mediates switching between invasion and  
1516 proliferation downstream of TGF $\beta$  in claudin-low breast tumor cells. *Oncogene* **34**, 2721–  
1517 2731 (2015).

1518 52. Pijnenborg, R., Dixon, G., Robertson, W. B. & Brosens, I. Trophoblastic invasion of  
1519 human decidua from 8 to 18 weeks of pregnancy. *Placenta* **1**, 3–19 (1980).

1520 53. Brosens, I., Robertson, W. B. & Dixon, H. G. The physiological response of the vessels  
1521 of the placental bed to normal pregnancy. *J. Pathol. Bacteriol.* **93**, 569–579 (1967).

1522 54. Burton, G. J., Jauniaux, E. & Watson, A. L. Maternal arterial connections to the placental  
1523 intervillous space during the first trimester of human pregnancy: the Boyd collection  
1524 revisited. *Am. J. Obstet. Gynecol.* **181**, 718–724 (1999).

1525 55. Sheridan, M. A. *et al.* Establishment and differentiation of long-term trophoblast organoid  
1526 cultures from the human placenta. *Nat. Protoc.* **15**, 3441–3463 (2020).

1527 56. Blankenship, T. N., Enders, A. C. & King, B. F. Trophoblastic invasion and the

1528 development of uteroplacental arteries in the macaque: immunohistochemical  
1529 localization of cytokeratins, desmin, type IV collagen, laminin, and fibronectin. *Cell Tissue  
1530 Res.* **272**, 227–236 (1993).

1531 57. King, A. & Loke, Y. W. Differential expression of blood-group-related carbohydrate  
1532 antigens by trophoblast subpopulations. *Placenta* **9**, 513–521 (1988).

1533 58. Smith, G. C. S. First-trimester determination of complications of late pregnancy. *JAMA:*  
1534 *the journal of the American Medical Association* vol. 303 561–562 (2010).

1535 59. Carter, A. M. Comparative studies of placentation and immunology in non-human  
1536 primates suggest a scenario for the evolution of deep trophoblast invasion and an  
1537 explanation for human pregnancy disorders. *Reproduction* **141**, 391–396 (2011).

1538 60. Kenny Roberts, L. T. Embedding and freezing fresh human tissue in OCT using  
1539 isopentane V.3. *protocols.io* (2019) doi:10.17504/protocols.io.95mh846.

1540 61. Krishnaswami, S. R. *et al.* Using single nuclei for RNA-seq to capture the transcriptome  
1541 of postmortem neurons. *Nat. Protoc.* **11**, 499–524 (2016).

1542 62. Bayraktar, O. A. *et al.* Astrocyte layers in the mammalian cerebral cortex revealed by a  
1543 single-cell *in situ* transcriptomic map. *Nat. Neurosci.* (2020) doi:10.1038/s41593-020-  
1544 0602-1.

1545 63. Popescu, D.-M. *et al.* Decoding human fetal liver haematopoiesis. *Nature* **574**, 365–371  
1546 (2019).

1547 64. Heaton, H. *et al.* Souporcell: robust clustering of single-cell RNA-seq data by genotype  
1548 without reference genotypes. *Nat. Methods* **17**, 615–620 (2020).

1549 65. Park, J.-E. *et al.* A cell atlas of human thymic development defines T cell repertoire  
1550 formation. *Science* **367**, (2020).

1551 66. Cusanovich, D. A. *et al.* A Single-Cell Atlas of In Vivo Mammalian Chromatin  
1552 Accessibility. *Cell* **174**, 1309–1324.e18 (2018).

1553 67. Gaspar, J. M. Improved peak-calling with MACS2. doi:10.1101/496521.

1554 68. Kleshchevnikov, V. *et al.* Comprehensive mapping of tissue cell architecture via  
1555 integrated single cell and spatial transcriptomics. *Cold Spring Harbor Laboratory*

1556 2020.11.15.378125 (2020) doi:10.1101/2020.11.15.378125.

1557 69. Kats, I., Vento-Tormo, R. & Stegle, O. SpatialDE2: Fast and localized variance  
1558 component analysis of spatial transcriptomics. doi:10.1101/2021.10.27.466045.

1559 70. González-Blas, C. B. *et al.* cisTopic: cis-regulatory topic modeling on single-cell ATAC-  
1560 seq data. *Nat. Methods* **16**, 397–400 (2019).

1561 71. Bravo González-Blas, C. *et al.* Identification of genomic enhancers through spatial  
1562 integration of single-cell transcriptomics and epigenomics. *Mol. Syst. Biol.* **16**, e9438  
1563 (2020).

1564 72. Wolf, F. A. *et al.* PAGA: graph abstraction reconciles clustering with trajectory inference  
1565 through a topology preserving map of single cells. *Genome Biol.* **20**, 59 (2019).

1566 73. Optimization, N. Jorge Nocedal Stephen J. Wright.

1567 74. TensorFlow. doi:10.5281/zenodo.6519082.

1568 75. Zhang, B. *et al.* Human placental cytotrophoblast epigenome dynamics over gestation  
1569 and alterations in placental disease. *Dev. Cell* **56**, 1238–1252.e5 (2021).

1570 76. Efremova, M., Vento-Tormo, M., Teichmann, S. A. & Vento-Tormo, R. CellPhoneDB:  
1571 inferring cell-cell communication from combined expression of multi-subunit ligand-  
1572 receptor complexes. *Nat. Protoc.* **15**, 1484–1506 (2020).

1573 77. Garcia-Alonso, L., Holland, C. H., Ibrahim, M. M., Turei, D. & Saez-Rodriguez, J.  
1574 Benchmark and integration of resources for the estimation of human transcription factor  
1575 activities. *Genome Res.* **29**, 1363–1375 (2019).

1576 78. Alvarez, M. J. *et al.* Functional characterization of somatic mutations in cancer using  
1577 network-based inference of protein activity. *Nat. Genet.* **48**, 838–847 (2016).

1578 79. Holland, C. H. *et al.* Robustness and applicability of transcription factor and pathway  
1579 analysis tools on single-cell RNA-seq data. *Genome Biol.* **21**, 36 (2020).

1580 80. Schep, A. N., Wu, B., Buenrostro, J. D. & Greenleaf, W. J. chromVAR: inferring  
1581 transcription-factor-associated accessibility from single-cell epigenomic data. *Nat.*  
1582 *Methods* **14**, 975–978 (2017).

1583 81. Khan, A. *et al.* JASPAR 2018: update of the open-access database of transcription factor

1584 binding profiles and its web framework. *Nucleic Acids Res.* **46**, D260–D266 (2018).

1585 82. Kulakovskiy, I. V. *et al.* HOCOMOCO: expansion and enhancement of the collection of

1586 transcription factor binding sites models. *Nucleic Acids Res.* **44**, D116–25 (2016).

1587 83. Pachkov, M., Erb, I., Molina, N. & van Nimwegen, E. SwissRegulon: a database of

1588 genome-wide annotations of regulatory sites. *Nucleic Acids Research* vol. 35 D127–

1589 D131 (2007).

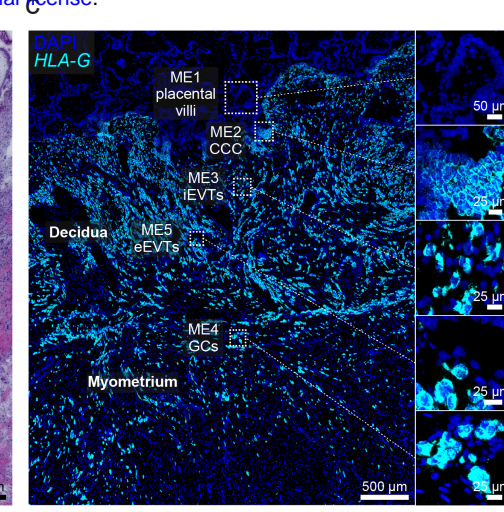
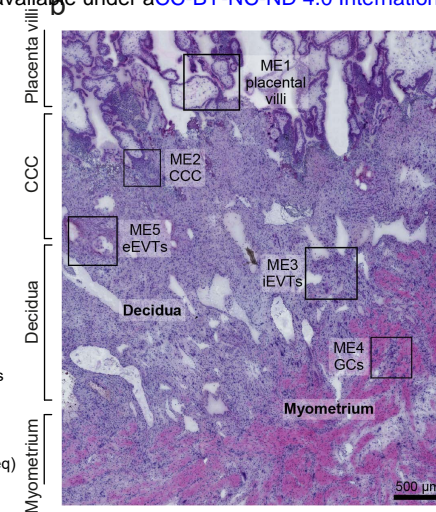
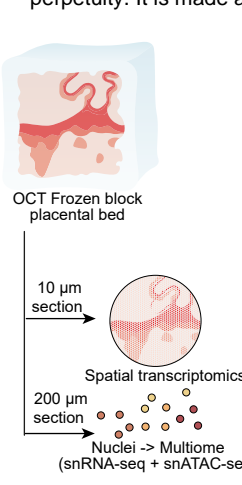
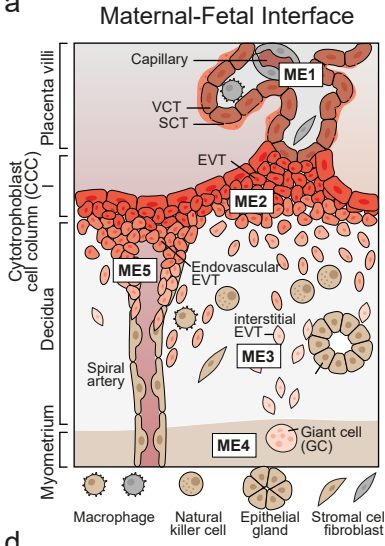
1590 84. Heinz, S. *et al.* Simple combinations of lineage-determining transcription factors prime

1591 cis-regulatory elements required for macrophage and B cell identities. *Mol. Cell* **38**, 576–

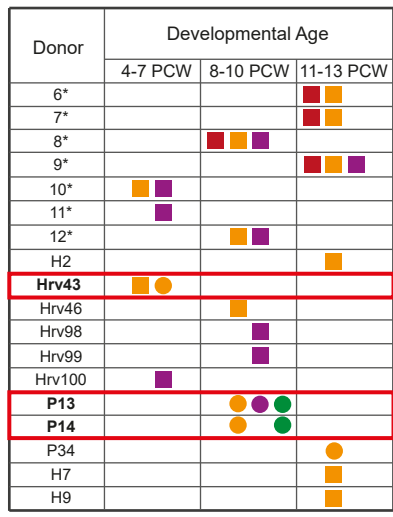
1592 589 (2010).

**Figure 1** bioRxiv preprint doi: <https://doi.org/10.1101/2022.11.06.515326>; this version posted November 6, 2022. The copyright holder for this preprint (which was not certified by peer review) is the author/funder, who has granted bioRxiv a license to display the preprint in perpetuity. It is made available under aCC-BY-NC-ND 4.0 International license.

a



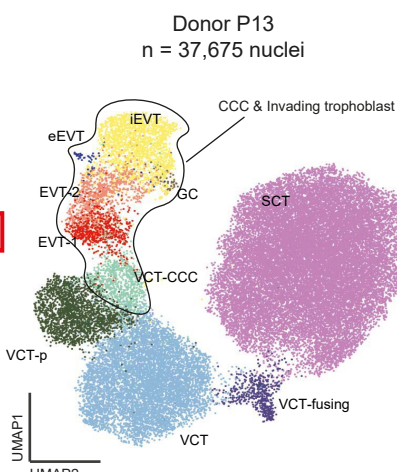
d



Tissue  
Blood  
Decidua basalis  
Placenta  
Myometrium

■ scRNA-seq  
○ snRNA-seq  
Spatial Transcriptomics + Multimodal

e

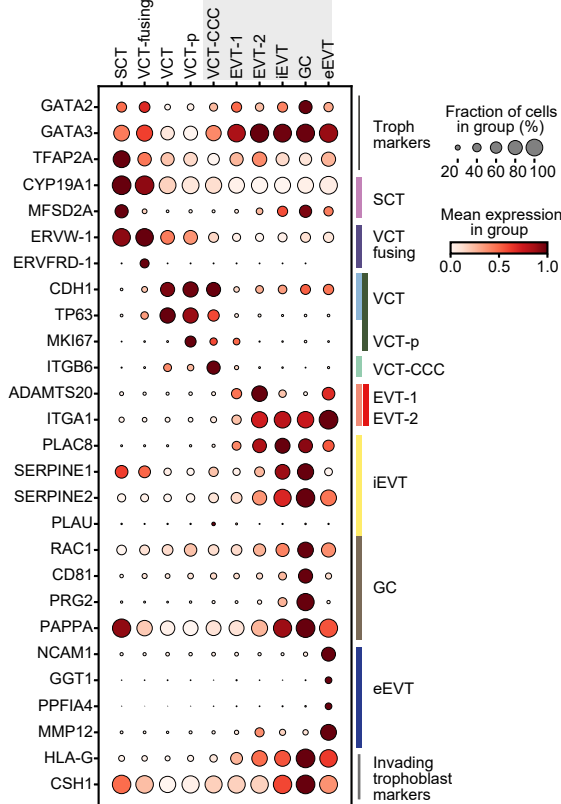


\*

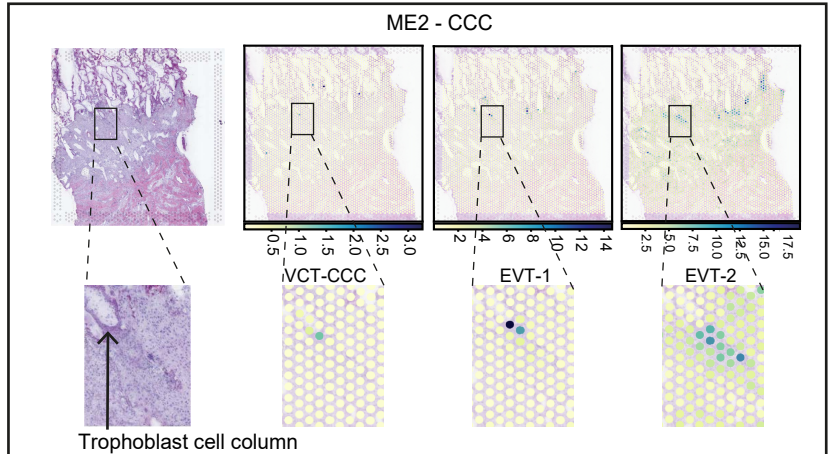
from Vento-Tormo et al

Nature 2018

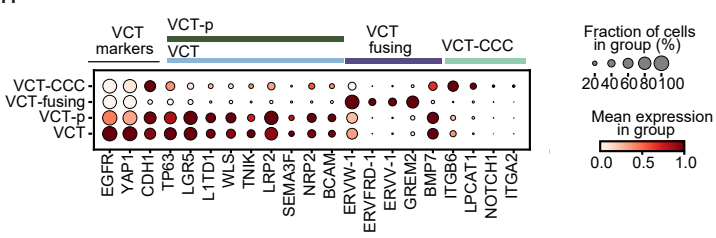
g Placenta Decidua/myometrium



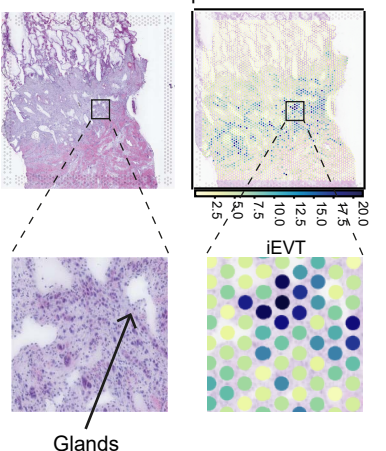
f



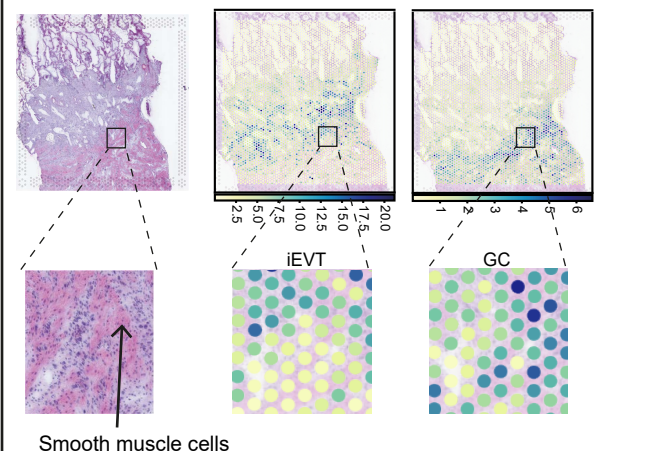
h



ME2 - CCC



ME4 - GC fusion



ME5 - Arteries

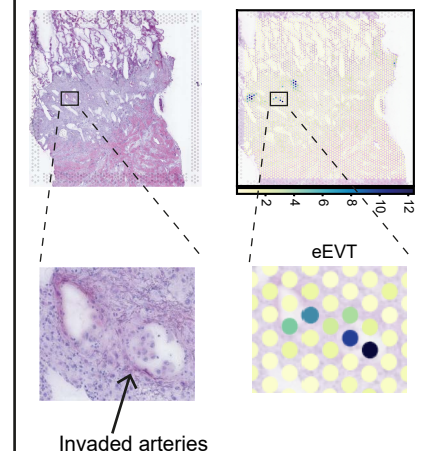
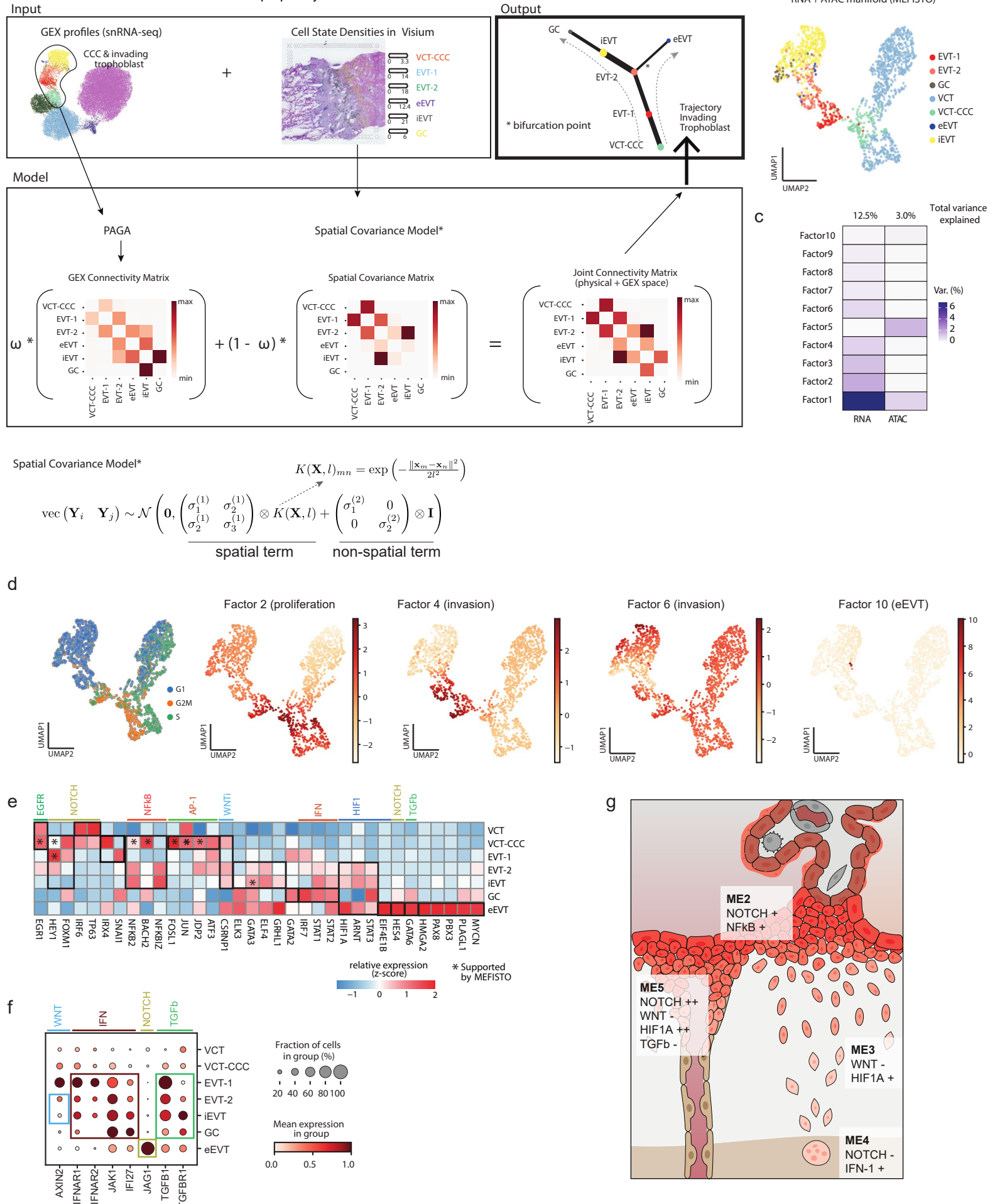


**Figure 2** bioRxiv preprint doi: <https://doi.org/10.1101/2022.11.06.515326>; this version posted November 6, 2022. The copyright holder for this preprint (which was not certified by peer review) is the author/funder, who has granted bioRxiv a license to display the preprint in perpetuity. It is made available under aCC-BY-NC-ND 4.0 International license.



bioRxiv preprint doi: <https://doi.org/10.1101/2022.11.06.515326>; this version posted November 6, 2022. The copyright holder for this preprint (which was not certified by peer review) is the author/funder, who has granted bioRxiv a license to display the preprint in perpetuity. It is made available under a [aCC-BY-NC-ND 4.0 International license](#).

growing media  
● EVTM  
● TOM

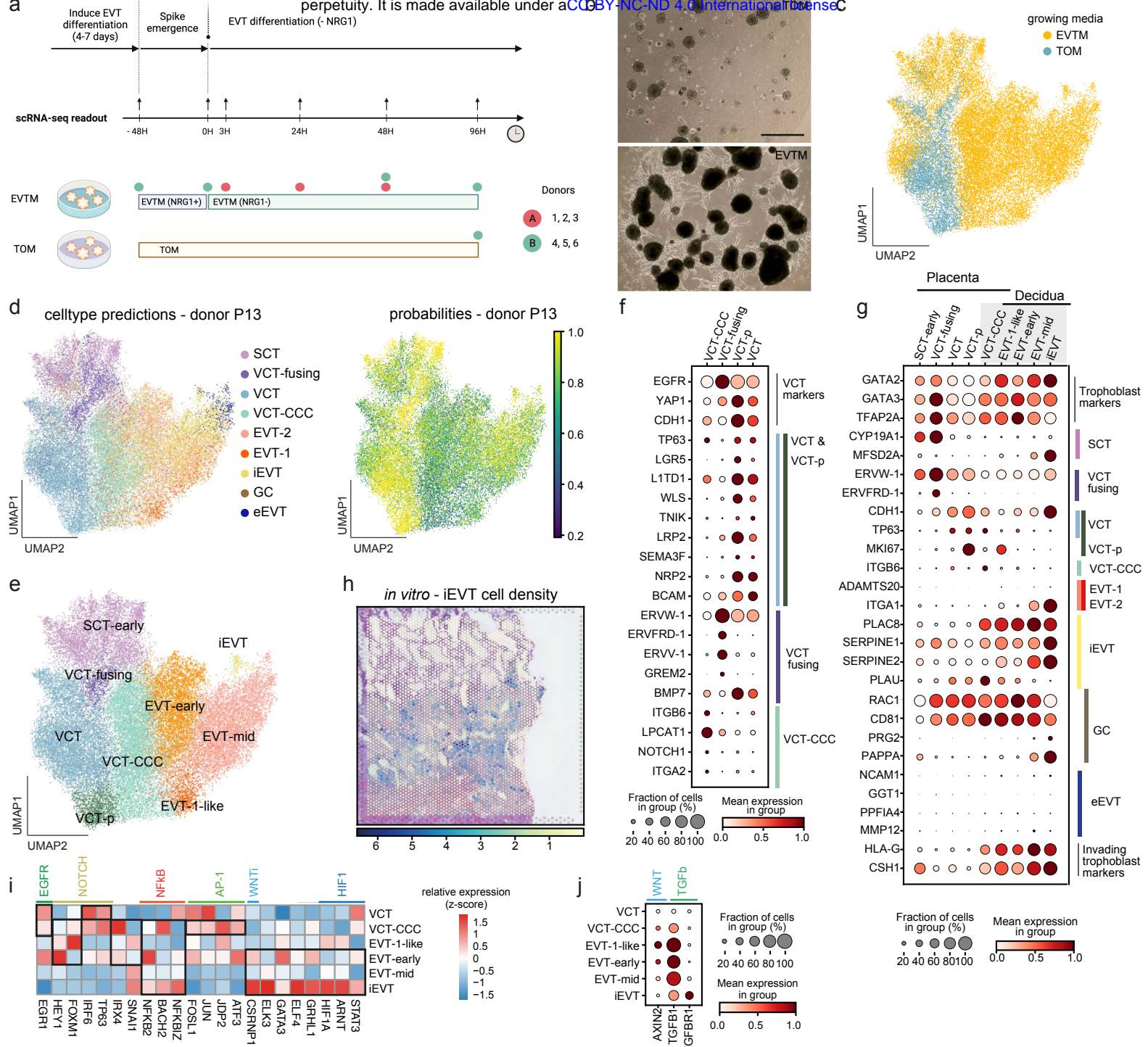
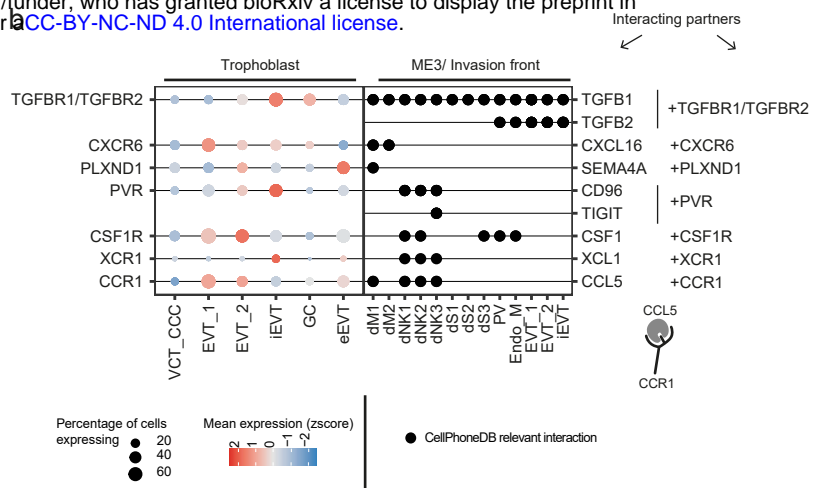
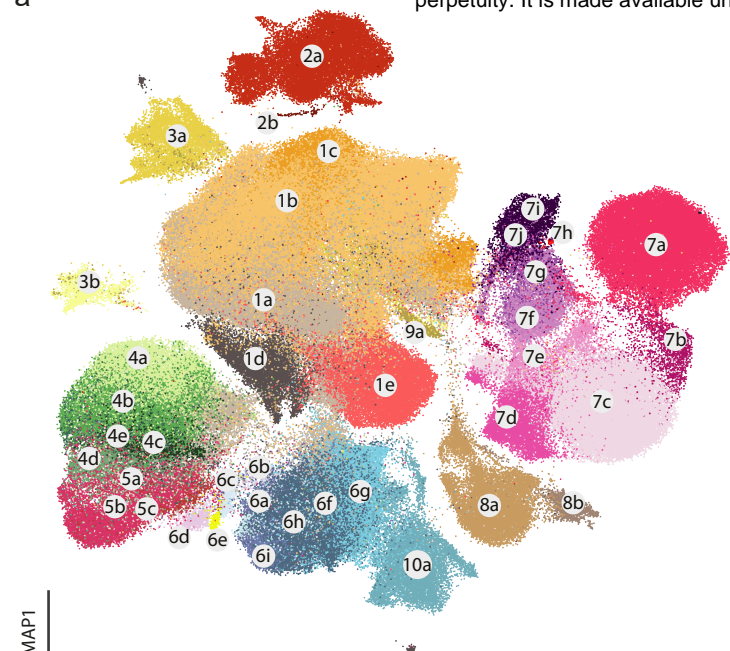
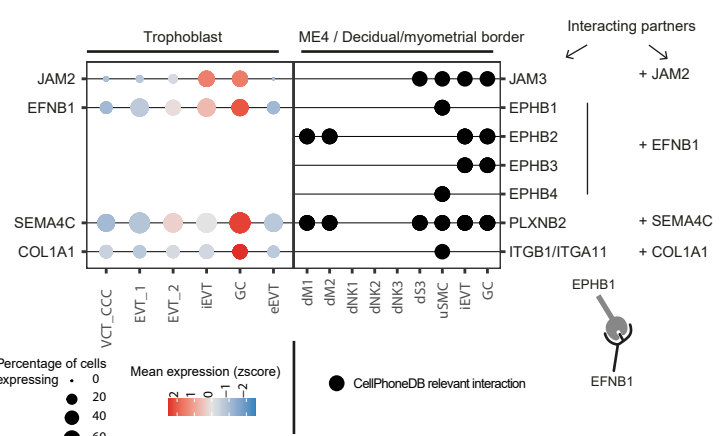


**Figure 4** bioRxiv preprint doi: <https://doi.org/10.1101/2022.11.06.515326>; this version posted November 6, 2022. The copyright holder for this preprint (which was not certified by peer review) is the author/funder, who has granted bioRxiv a license to display the preprint in perpetuity. It is made available under aCC-BY-NC-ND 4.0 International license.

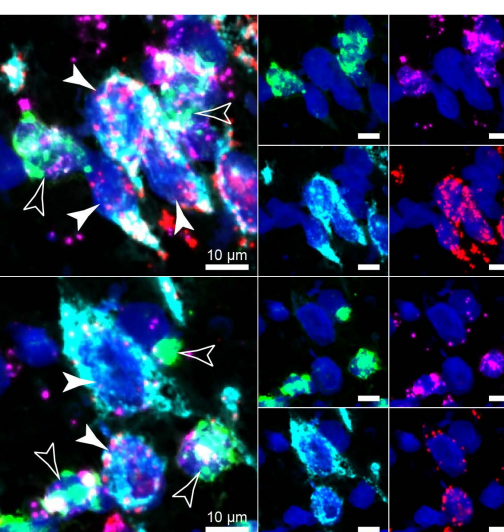
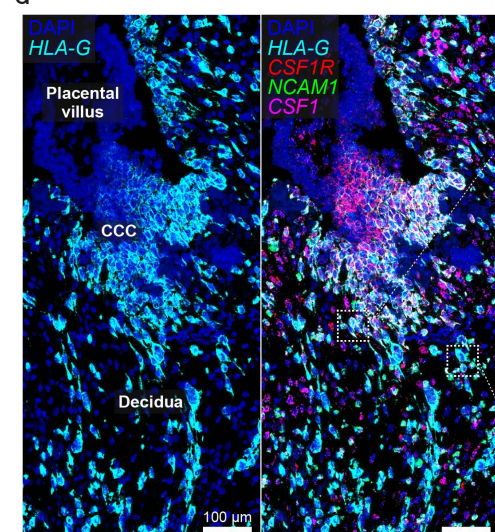
a



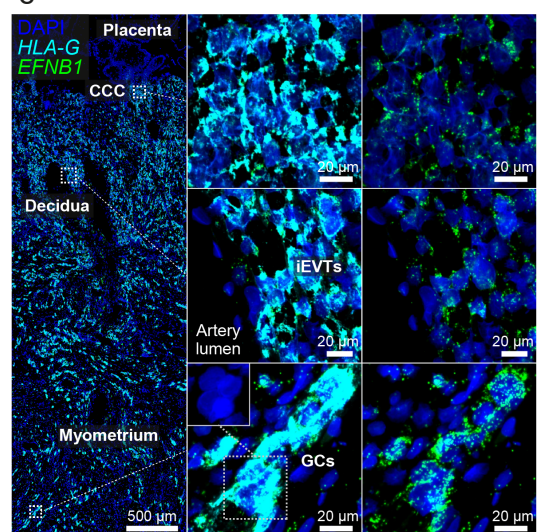
c



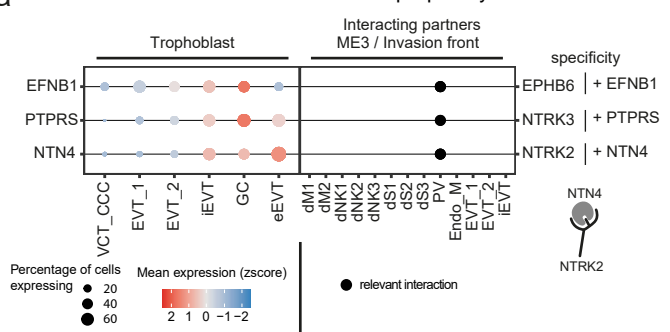
d



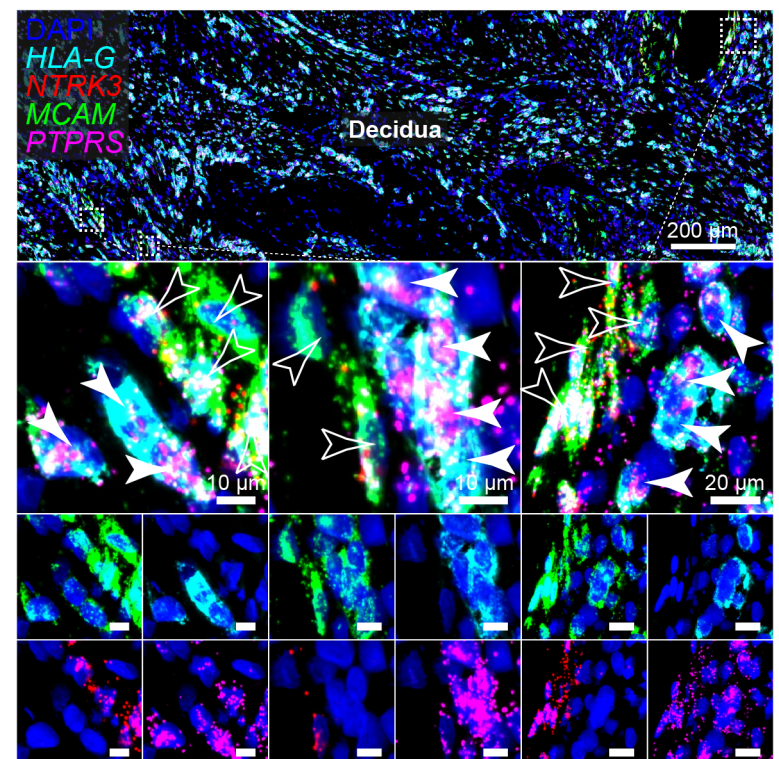
e



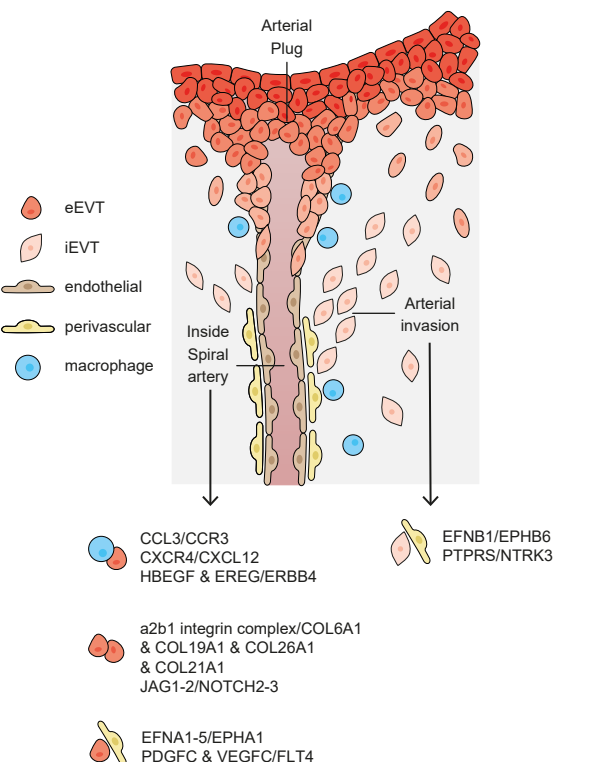
a



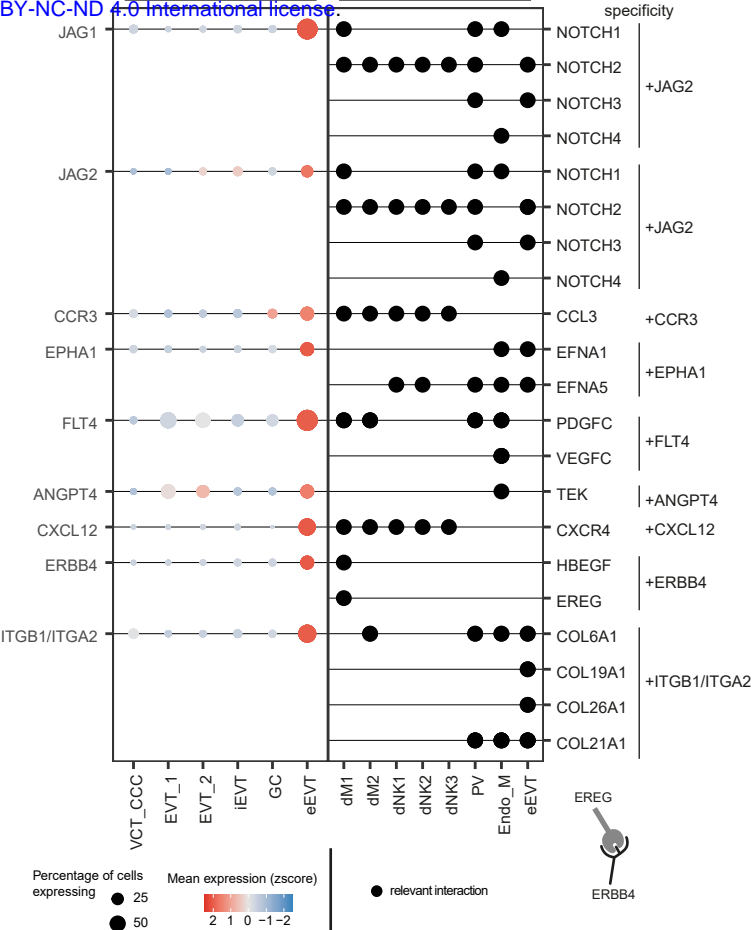
b



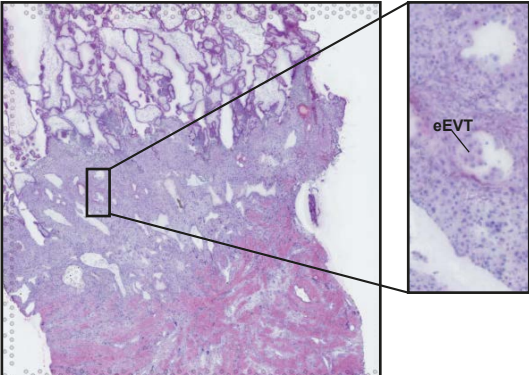
f



c



d



e

